

# Master's Thesis

## *Optimisation and Benchmarking of a Terahertz Time-Domain Spectrometer*

Mathias Hedegaard Kristensen

June 2017



Department of Physics and Nanotechnology  
Aalborg University  
Skjernvej 4A  
9220 Aalborg East





# AALBORG UNIVERSITET

## STUDENTERRAPPORT

### Department of Physics and Nanotechnology

Aalborg University  
Skjernvej 4A  
9220 Aalborg East  
Telefon 99 40 92 15  
Fax 99 40 92 35  
[Http://nano.aau.dk](http://nano.aau.dk)

**Title:**

Optimisation and Benchmarking of a Terahertz Time-Domain Spectrometer

**Theme:**

Master's Thesis

**Project Period:**

Spring semester 2017

**Project Group:**

5.211

**Participant(s):**

Mathias Hedegaard Kristensen

**Supervisor(s):**

Esben Skovsen

**Copies: 3****Page Numbers: 54****Date of Completion:**

June 8, 2017

**Synopsis:**

The aim of this project has been to optimise and benchmark the terahertz (THz) time-domain spectrometer based on broadband THz pulses generated and detected by photoconductive antennas, which was designed and constructed during my ninth semester in the autumn of 2016.

The theoretical foundations are laid starting from Maxwell's equations through the general technique of THz time-domain spectroscopy to the specific mechanisms behind generation and detection of broadband THz pulses utilising photoconductive antennas, before the data analysis and lock-in amplification is treated.

First, the spectrometer design and the data acquisition was adjusted. Subsequently, software was developed for easier and more consistent analysis of the data. The settings of the spectrometer including the lock-in amplifier was tested to provide a default initial settings for spectrometric experiments. Finally, a benchmarked by characterisation of the narrow and strong absorption signature of  $\alpha$ -lactose monohydrate powder at 0.53 THz was carried out followed by a performance evaluation.

The spectrometer is found to function properly within a bandwidth ranging from 0.2 to  $\sim$ 1.4 THz limited by the THz source. The ensuing data analysis is also found to be implemented correctly.



# Contents

<b>Preface</b>	<b>vii</b>
<b>Danish Summary</b>	<b>ix</b>
<b>1 Introduction</b>	<b>1</b>
<b>2 Theoretical Foundations</b>	<b>3</b>
2.1 Maxwell's Macroscopic Equations . . . . .	3
2.1.1 The Wave Equation . . . . .	3
2.1.2 Reflection and Transmission . . . . .	6
2.2 Terahertz Time-Domain Spectroscopy . . . . .	8
2.2.1 Photoconductive Generation of Broadband Terahertz Pulses . . . . .	9
2.2.2 Photoconductive Detection of Broadband Terahertz Pulses . . . . .	13
2.2.3 Data Analysis in Terahertz Transmission Spectroscopy . . . . .	16
2.3 Lock-in Amplification . . . . .	25
<b>3 Terahertz Time-Domain Spectrometer</b>	<b>29</b>
3.1 Spectrometer Design . . . . .	29
3.2 Data Acquisition and Analysis . . . . .	31
3.3 Lock-in Amplifier and Scan Settings . . . . .	34
3.4 Benchmarking by Terahertz Absorption Spectra . . . . .	41
3.5 Spectrometer Performance . . . . .	47
<b>4 Conclusion and Outlook</b>	<b>51</b>
<b>Bibliography</b>	<b>53</b>



# Preface

This master's thesis is authored by Mathias Hedegaard Kristensen on the tenth semester in the spring of 2017 at the Department of Physics and Nanotechnology, Aalborg University, Denmark.

The thesis is in continuation of my ninth semester project found in [1], which dealt with the design and construction of a terahertz time-domain spectrometer, and concerns the optimisation and benchmarking of the spectrometer. The reader of this paper is supposed to have basic literacy concerning optics and solid-state physics.

The citations throughout this paper are referred to by the Vancouver system, i.e. each citation is given a number, e.g. [1], within the text that refers to a numbered entry in the Bibliography found at the back of the thesis.

The theoretical computations and the experimental data analysis made during the thesis were executed utilising the commercial software MATLAB 2016b.

I would like to thank Esben Skovsen for kind supervision, for passing on his knowledge and experiences, and for always being very forthcoming. Also big thanks are given to Peter Kjær Kristensen for repairing the terahertz source and assisting with equipment in the lab, to Karina Boller Jensen for reintroducing me to the biolab and procuring the right powders needed for the benchmark, and finally, to Christian Buhl Sørensen for discussing various issues related to both theoretical and experimental work with me.

Aalborg University, June 8, 2017



## Danish Summary

Dette kandidatspeciale er skrevet som videreførelse af mit niende semesters projekt sidste semester, hvor et terahertz (THz) tidsdomæne spektrometer blev udviklet og opbygget.

Terahertzstråling er elektromagnetisk stråling med frekvenser liggende mellem det fjerninfrarøde bånd og mikrobølgebåndet. Terahertzteknologien er ung, og specielt spektroskopi og billeddannelse ved hjælp af THz-stråling er i hastig udvikling og har potentielt mange anvendelsesmuligheder inden for sikkerhedssystemer, detektion af sprængstoffer og narkotika, inline-overvågning af polymere materialer, biomedicinsk billeddannelse etc.

THz-stråling kan genereres og detekteres på flere forskellige måder, men en fælles udfordring er, at store stationære systemer er nødvendige. Der forskes derfor bredt i udfærdigelsen af kompakte, intense, og effektive THz-kilder. Dette projekt er begrænset til spektroskopi med bredbåndet THz-pulser genereret og detekteret med fotoledende antenner.

Formålet med denne afhandling har været at optimere og verificere pålideligheden af spektrometret opbygget i løbet af niende semester, så det senere kan bruges til at karakterisere forskellige antennedesign til fotoledende terahertz kilder samt til at karakterisere effekten af de forskellige antenneparametre.

I første del af afhandlingen værende Kapitel 2 er det teoretiske grundlag udfærdiget. Med udgangspunkt i den klassiske elektromagnetisme beskrives vekselvirkningerne mellem THz-stråling og stof af Maxwells ligninger, hvorefter de grundlæggende principper bag THz-tidsdomæne spektroskopi (THz-TDS) forklares og diskuteres. Derfra følger en kort og præcis beskrivelse af virkemåden og mekanismerne bag generering og detektering af bredbåndet THz-pulser ved hjælp af fotoledende antenner. Efterfølgende behandles dataanalysen relateret til THz-transmissionsspektroskopi, og forskellige indgangsvinkler her til afdækkes. Den teoretiske del afsluttes med en udtømmende diskussion af lock-in-forstærkningsprincippet.

Anden del behandler i Kapitel 3 det eksperimentelle arbejde udført gennem projektperioden fra februar til juni 2017. Indledningsvist præsenteres det oprindelige spektrometerdesign, som det så ud ved afslutningen af niende semester, hvorefter det optimerede design præsenteres og diskuteres. Herefter følger en kort beskrivelse af softwaren, der er blevet udarbejdet til opsamling af data og til dataanalyse. Der er udført en række test af effekten af de forskellige indstillinger af spektrometret inklusiv lock-in-forstærkeren for at nå frem til et sæt standardindstillinger, som kan finjusteres til konkrete spektroskopiske målinger. For at verificere pålideligheden af spektrometret udføres en benchmarktest i form af karakterisering af absorptionssignaturen for  $\alpha$ -lactosemonohydrat ved 0,53 THz. Det lykkes at karakterisere lactoseprøven med høj præcision, og både absorptionensignaturens centerfrekvens samt linjebredde eftervises med lav usikkerhed. Den overordnede ydeevne af spektrometret undersøges nærmere, da THz-kilden udviser tegn på beskadigelse.

Slutteligt samles erfaringerne igennem projektet og en overordnet konklusion gives i Kapitel 4.



# 1. Introduction

Terahertz (THz) radiation is electromagnetic radiation with frequencies  $\nu$  spanning the region between the far-infrared band and the microwave band of the electromagnetic spectrum. A brief introduction of the field of science and some of its applications as well as the motivation of this thesis will be given in the following chapter, which is inspired by [2; 3; 4].

The THz band is commonly defined to span from 0.1 to 10 THz corresponding to wavelengths  $\lambda$  of 30  $\mu\text{m}$  to 3 mm. This definition will also apply in this work. There are a few units at  $\nu = 1$  THz that are worth noting; period  $\tau = 1/\nu = 1$  ps, wavelength  $\lambda = c/\nu = 300 \mu\text{m}$ , and photon energy  $h\nu = 4.14$  meV, this is three orders of magnitude smaller than the energy required to ionise an atom [4]. Here  $c = 3.00$  m/s is the speed of light in vacuum and  $h = 6.63 \cdot 10^{-34}$  Js is the Planck constant.

THz technologies have just matured and develop in a rapid pace. The field is still in a transition phase, where research foci are moving towards more practical applications. So far, THz spectroscopy and imaging have promising applications within security imaging, detection of explosives and illegal drugs, inline monitoring of polymeric materials, biomedical imaging etc. Thus, the motivation of the field is clear.

The attractive properties of the THz band regarding condensed matter are found in the inherent grouping of materials. Liquid water is polar and highly absorptive at THz frequencies ( $\alpha \approx 250/\text{cm}$  at 1 THz), while nonpolar and nonmetallic materials (dielectrics) such as ceramics, clothes, paper, plastics, and wood are transparent at THz frequencies. Due to high electrical conductivity of metals, these are highly reflective at THz frequencies. Clearly, this can be exploited in numerous applications.

Absorption signatures of organic and biological molecules at THz frequencies are linked to inter-molecular interactions and large-amplitude vibrational motions. Thus, THz spectroscopy can be employed to detect e.g. explosives, test pharmaceutical products or investigate protein conformations. Furthermore, since the energy of THz radiation is too low to cause ionisation and the power levels in common THz systems are much lower than of the natural occurring THz radiation, no thermal effects that could damage the cells occur, THz light is considered safe for probing biological samples.

THz radiation can be generated and detected in different ways; for example by nonlinear optical processes or by time-varying currents induced by accelerating charges. In this thesis, only THz light generated and detected by mechanisms related to time-varying currents are emphasised. To be more precise, only generation and detection of broadband THz pulses utilising photoconductive antennas (PCAs) in a time-domain spectrometer (THz-TDS) are studied.

## Overview

An introduction to the theoretical foundations are given in Chapter 2. The framework of THz electromagnetic interactions with matter is formulated by Maxwell's equations from the classical electromagnetism. In the following sections, the principles of terahertz time-domain spectroscopy are explained, and a theoretical clarification of generation and detection of broadband THz pulses utilising photoconductive antennas is given. Next, it is

examined, how an analysis of THz transmission spectroscopy data is made correctly. The chapter is completed by a theoretical description of the lock-in amplification technique.

In Chapter 3, the experimental work is propound. An introduction of the spectrometer setup and the improvements that have been made during this thesis to optimise the spectrometer is given. The data acquisition and data analysis software are briefly described in the subsequent section. Before any spectrometric results are produced, the settings of the spectrometer including the lock-in amplifier are optimised to attain a set of default settings. Finally, spectrometric measurements of  $\alpha$ -lactose monohydrate are carried out and analysed to underpin the reliability of the setup. The spectrometer performance is concludingly investigated on the basis of the acquired results.

In closing, Chapter 4 summarises the results and conclusions of this thesis, and gives an outlook on future research options.

## 2. Theoretical Foundations

In this chapter inspired by [1; 5; 2; 6] the theoretic fundamentals are made starting from Maxwell's equations over transmission and reflection optics of Fresnel through the basic principles of terahertz time-domain spectroscopy to a theoretical discussion of the mechanisms in photoconductive terahertz sources and detectors and finally the subsequent data analysis.

### 2.1 Maxwell's Macroscopic Equations

THz radiation is electromagnetic waves, and thus, described by Maxwell's macroscopic equations

$$\vec{\nabla} \cdot \vec{D} = \rho_f, \quad (2.1)$$

$$\vec{\nabla} \cdot \vec{B} = 0, \quad (2.2)$$

$$\vec{\nabla} \times \vec{E} = -\frac{\partial \vec{B}}{\partial t}, \quad (2.3)$$

$$\vec{\nabla} \times \vec{H} = \vec{J}_f + \frac{\partial \vec{D}}{\partial t}, \quad (2.4)$$

as any other electromagnetic wave in matter, where  $\rho_f$  in Gauss's law is the free charge density and  $\vec{J}_f$  in the Maxwell-Ampère equation is the free current density. The macroscopic fields, the electric displacement field  $\vec{D}$  and the magnetic  $\vec{H}$  field, are defined through the fundamental electric and magnetic fields  $\vec{E}$  and  $\vec{B}$  as

$$\vec{D} \equiv \varepsilon_0 \vec{E} + \vec{P} = \varepsilon \vec{E}, \quad (2.5)$$

$$\vec{H} \equiv \frac{1}{\mu_0} \vec{B} - \vec{M} = \frac{1}{\mu} \vec{B}, \quad (2.6)$$

where  $\varepsilon_0$  is the vacuum permittivity and  $\mu_0$  is the vacuum permeability. The electromagnetic properties of matter on the macroscopic scale is accounted for by the polarisation  $\vec{P}$  and the magnetisation  $\vec{M}$ . Note that the identities in Eqs. (2.5) and (2.6) including the electric permittivity  $\varepsilon$  and the magnetic permeability  $\mu$  only are valid in isotropic and linear media. Finally, including the Lorentz force law

$$\vec{F} = q(\vec{E} + \vec{v} \times \vec{B}), \quad (2.7)$$

where  $q$  is the charge of a particle moving with velocity  $\vec{v}$  in the presence of an electric field  $\vec{E}$  and a magnetic field  $\vec{B}$ , with the apparently simple Maxwell equations the well-known theoretical foundation of classical electrodynamics is established.

#### 2.1.1 The Wave Equation

The electromagnetic wave equations

$$\vec{\nabla} \times (\vec{\nabla} \times \vec{E}) + \varepsilon \mu \frac{\partial^2 \vec{E}}{\partial t^2} = -\mu \frac{\partial \vec{J}_f}{\partial t}, \quad (2.8)$$

$$\vec{\nabla} \times (\vec{\nabla} \times \vec{H}) + \varepsilon \mu \frac{\partial^2 \vec{H}}{\partial t^2} = \vec{\nabla} \times \vec{J}_f, \quad (2.9)$$

are achieved from Eqs. (2.3) and (2.4) by disentangling the electric and magnetic fields through the curl operation and utilising the identities in Eqs. (2.5) and (2.6). These wave equations can be simplified if the vector identity

$$\vec{\nabla} \times (\vec{\nabla} \times \vec{F}) = \vec{\nabla}(\vec{\nabla} \cdot \vec{F}) - \nabla^2 \vec{F} \quad (2.10)$$

is applied;

$$\nabla^2 \vec{E} - \varepsilon\mu \frac{\partial^2 \vec{E}}{\partial t^2} = \mu \frac{\partial \vec{J}}{\partial t} + \frac{1}{\varepsilon} \vec{\nabla} \rho_f, \quad (2.11)$$

$$\nabla^2 \vec{H} - \varepsilon\mu \frac{\partial^2 \vec{H}}{\partial t^2} = -\vec{\nabla} \times \vec{J}_f. \quad (2.12)$$

Neglecting fluctuations in the charge density, i.e.  $\vec{\nabla} \rho_f = 0$ , and assuming the free current density is linear with the electric field through the electric conductivity  $\sigma$  simplifies the electric wave equation further as

$$\nabla^2 \vec{E} = \sigma\mu \frac{\partial \vec{E}}{\partial t} + \varepsilon\mu \frac{\partial^2 \vec{E}}{\partial t^2}, \quad (2.13)$$

where  $\sigma$  and  $\varepsilon$  are real and independent. Through Eq. (2.3) the magnetic wave equation simplifies identically. Thus, if one of the time-varying fields are known, the other follows immediately from Maxwell's equations due to the entangled nature of the fields forming an electromagnetic wave.

In dielectric or insulating media the wave equation takes the form

$$\nabla^2 \vec{E} = \varepsilon\mu \frac{\partial^2 \vec{E}}{\partial t^2} = \frac{1}{v^2} \frac{\partial^2 \vec{E}}{\partial t^2}. \quad (2.14)$$

Thus, electromagnetic waves propagate through nonmagnetic ( $\mu = \mu_0$ ) homogeneous media at a speed

$$v = \frac{1}{\sqrt{\varepsilon\mu}} = \frac{c}{n}, \quad (2.15)$$

where  $c = 1/\sqrt{\varepsilon_0\mu_0}$  is the speed of light in vacuum and  $n = \sqrt{\varepsilon/\varepsilon_0}$  is the refractive index.

Linearly-polarised monochromatic plane waves with wave vector  $\vec{k}$  and angular frequency  $\omega$  are general solutions of the wave equations, i.e.

$$\vec{E}(\vec{r}, t) = \vec{E}_0 e^{i(\vec{k} \cdot \vec{r} - \omega t)} \quad \text{and} \quad \vec{H}(\vec{r}, t) = \vec{H}_0 e^{i(\vec{k} \cdot \vec{r} - \omega t)}. \quad (2.16)$$

The relations

$$\vec{k} \cdot \vec{E} = 0 \quad \text{and} \quad \vec{k} \cdot \vec{H} = 0 \quad (2.17)$$

are obtained by substituting the general solutions into Maxwell's equations

$$\vec{\nabla} \cdot \vec{E} = 0 \quad \text{and} \quad \vec{\nabla} \cdot \vec{B} = 0. \quad (2.18)$$

From the relations in Eq. (2.17) it is clear that both  $\vec{E}$  and  $\vec{H}$  are perpendicular to the wave vector  $\vec{k}$  implying transverse electromagnetic waves. The fields of an electromagnetic wave is associated by the relation

$$\vec{k} \times \vec{E} = \omega\mu\vec{H} \quad (2.19)$$

## 2.1. Maxwell's Macroscopic Equations

deduced from Eq. (2.3). The electromagnetic properties of a medium  $\varepsilon$  and  $\mu$  governs how an electromagnetic wave propagates in the medium through the dispersion relation

$$k^2 = \varepsilon\mu\omega^2. \quad (2.20)$$

This relation is simply obtained by inserting the plane wave solution into the wave Eq. (2.14). For a nonmagnetic medium, where  $\mu = \mu_0$ , this can be rewritten as

$$k = n\frac{\omega}{c} = \frac{2\pi}{\lambda}, \quad (2.21)$$

where  $\omega = 2\pi f$  and wavelength  $\lambda = v/f$  associated with frequency  $f$ .

The directional energy flux density of an electromagnetic wave is given by Poynting vector

$$\vec{S} = \vec{E} \times \vec{H}. \quad (2.22)$$

To calculate the energy flux the fields are assumed to be time-harmonic with complex amplitudes and the Poynting vector is time-averaged, thus,

$$\langle \vec{S} \rangle = \langle \vec{E} \times \vec{H} \rangle = \langle \text{Re}(\vec{E}_0 e^{-i\omega t}) \times \text{Re}(\vec{H}_0 e^{-i\omega t}) \rangle \quad (2.23)$$

Utilising the identity  $\text{Re}(z) = \frac{1}{2}(z + z^*)$  with  $z^*$  as the complex conjugate of  $z$  and some algebra the result is

$$\langle \vec{S} \rangle = \frac{1}{T} \int_0^T \left\{ \frac{1}{2} \text{Re}(\vec{E}_0 \times \vec{H}_0^*) + \frac{1}{2} \text{Re}(\vec{E}_0 \times \vec{H}_0 e^{-i2\omega t}) \right\} dt. \quad (2.24)$$

The last term is second harmonic, and hence, averages to zero leaving

$$\langle \vec{S} \rangle = \frac{1}{2} \text{Re}(\vec{E}_0 \times \vec{H}_0^*). \quad (2.25)$$

An expression for  $\vec{H}$  can be deduced from Eq. (2.19) as

$$\vec{H}_0^* = \frac{k}{\omega\mu_0} \vec{e}_k \times \vec{E}_0, \quad (2.26)$$

where  $\vec{e}_k = \vec{k}/k$  is a unit vector in the direction of the wave propagation. Thus,

$$\vec{E}_0 \times (\vec{e}_k \times \vec{E}_0^*) = \vec{e}_k (\vec{E}_0 \cdot \vec{E}_0^*) - \vec{E}_0 (\vec{e}_k \cdot \vec{E}_0^*) = \vec{e}_k |\vec{E}_0|^2, \quad (2.27)$$

and the energy flux is given by

$$\langle \vec{S} \rangle = \frac{1}{2} \frac{k}{\omega\mu_0} |\vec{E}_0|^2 \vec{e}_k = \frac{1}{2} v\varepsilon |E_0|^2 \vec{e}_k. \quad (2.28)$$

Finally, the radiation intensity can be found as the magnitude of the time-averaged poynting vector, that is,

$$I = \left| \langle \vec{S} \rangle \right| = \frac{1}{2} v\varepsilon |E_0|^2, \quad (2.29)$$

which is often given in units of W/cm<sup>2</sup>.

In conductive media, the proper wave equation is Eq. (2.13), however, the plane waves in Eq. (2.16) are still valid solutions and even the relations in Eq. (2.17) holds, that is,

the electromagnetic waves are transverse. Inserting the general solution into the wave Eq. (2.13) one arrives at the dispersion relation

$$k^2 = i\omega\sigma\mu + \omega\varepsilon\mu. \quad (2.30)$$

The conductivity  $\sigma$  is much larger than  $\omega\varepsilon$ , and hence,

$$k^2 \approx i\sigma\mu\omega. \quad (2.31)$$

This implies that the magnitude of the wave vector is complex;

$$k = k_1 + ik_2 \approx \sqrt{\frac{\omega\mu\sigma}{2}}(1 + i). \quad (2.32)$$

Thus, when incident on a conducting medium the electromagnetic wave decays exponentially with attenuation length

$$\delta = \sqrt{\frac{2}{\omega\mu\sigma}}, \quad (2.33)$$

also referred to as the skin depth. As most metals behave like a perfect conductor for THz waves, the skin depth becomes very small, wherefore electromagnetic fields in the THz region decay rapidly when incident on conductive media as Figure 2.1 emphasises.

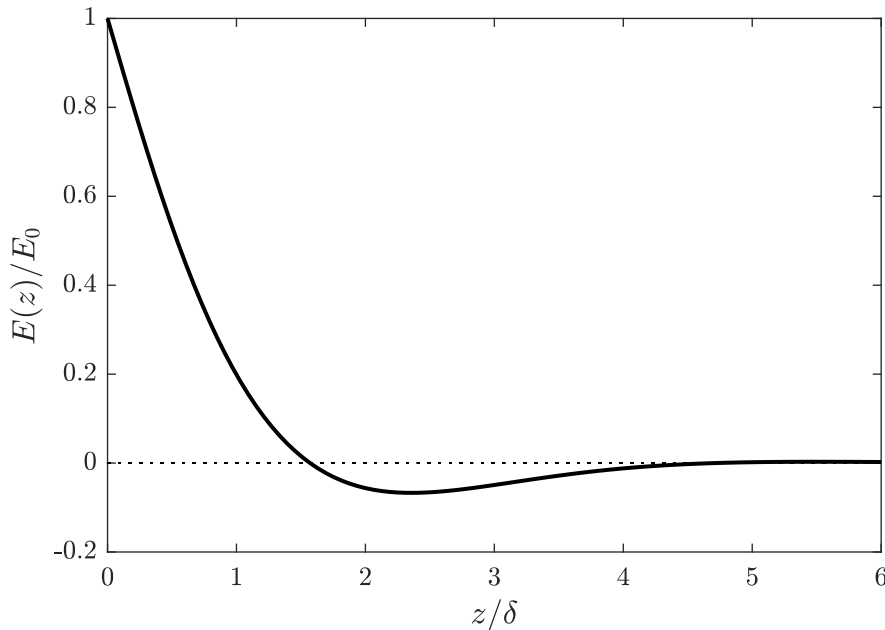


**Figure 2.1:** *Electric field decay in a conductor.*

### 2.1.2 Reflection and Transmission

Consider the case of an electromagnetic wave of incidence colliding with the interface of two linear dielectric media at  $z = 0$  as illustrated in Figure 2.2.

At the interface the wave of incidence is divided into two waves; the reflected wave propagating back into the original medium one and the transmitted wave propagating into medium two across the interface. First, the law of reflection determines the angle of incidence  $\theta_I$  equals the angle of reflection  $\theta_R$ , that is  $\theta_I = \theta_R = \theta_1$ . Next, the wave of transmission obeys Snell's law

$$n_1 \sin \theta_1 = n_2 \sin \theta_2, \quad (2.34)$$

## 2.1. Maxwell's Macroscopic Equations

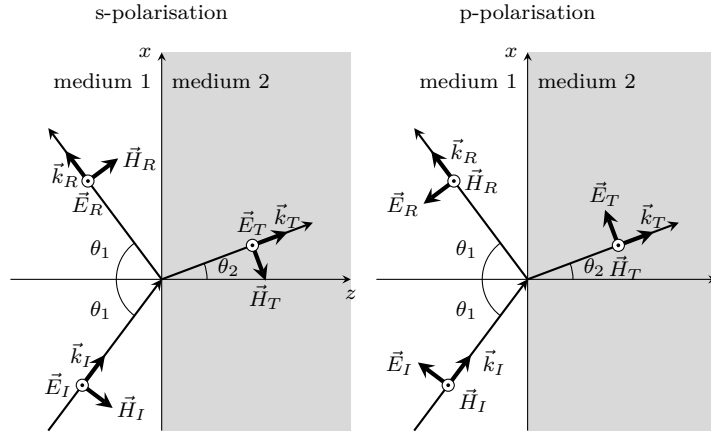


**Figure 2.2:** Illustration of the reflection and transmission of *s*- and *p*-polarised electromagnetic waves, respectively, incident onto an interface of two linear dielectric media.

where  $n_{1,2}$  are the refractive indices of the media and  $\theta_{1,2}$  are the angle of incidence and the angle of refraction, respectively. At the interface both the electric and the magnetic fields have to satisfy the boundary conditions implying continuous tangential components of both fields across the boundary. Since an electromagnetic wave is transverse the wave of incidence can be decomposed into two orthogonal polarisations. By convention, the *s*-polarisation  $\vec{E}_s$  indicates that the plane of incidence is spanned by the propagation vector  $\vec{k}_I$  of the incident wave and the normal vector of the interface, such that the electric field vector is perpendicular to the plane of incidence. The *p*-polarisation  $\vec{E}_p$  describes the complementary situation, where the electric field vector is parallel to the plane of incidence. Both situations are illustrated in Figure 2.2.

The tangential components are the components lying in the interface plane, which all electric components does when the wave of incidence is *s*-polarised and the electric boundary condition becomes

$$E_{I,s}(z=0) + E_{R,s}(z=0) = E_{T,s}(z=0). \quad (2.35)$$

The magnetic field vectors of the *s*-polarised waves all lie in the plane of incidence, thus, the magnetic boundary condition is

$$-H_{I,s}(z=0) \cos \theta_1 + H_{R,s}(z=0) \cos \theta_1 = -H_{T,s}(z=0) \cos \theta_2. \quad (2.36)$$

Here the signs reflects the directions of the tangential components in proportion to the  $x$  axis. From Maxwell's equation the relation  $H = \sqrt{\varepsilon/\mu}E$  was obtained, where  $\varepsilon$  and  $\mu$  are the electric permittivity and magnetic permeability of the medium of propagation. Now recall that  $n = c\sqrt{\varepsilon\mu}$  to arrive at the expressions of the magnetic field amplitudes

$$H_{I,R} = \frac{n_1}{\mu_1 c} E_{I,R} \quad \text{and} \quad H_T = \frac{n_2}{\mu_2 c} E_T. \quad (2.37)$$

Since both media are dielectric  $\mu_1 = \mu_2 = \mu_0$ , and thus, the magnetic boundary condition becomes

$$n_1(E_{I,s} - E_{R,s}) \cos \theta_1 = n_2 E_{T,s} \cos \theta_2. \quad (2.38)$$

Finally, when combining Eqs. (2.35) and (2.38) the Fresnel equations for *s*-polarised electromagnetic waves are achieved

$$r_s = \frac{E_{R,s}}{E_{I,s}} = \frac{n_1 \cos \theta_1 - n_2 \cos \theta_2}{n_1 \cos \theta_1 + n_2 \cos \theta_2} \quad \text{and} \quad t_s = \frac{E_{T,s}}{E_{I,s}} = \frac{2n_1 \cos \theta_1}{n_1 \cos \theta_1 + n_2 \cos \theta_2}. \quad (2.39)$$

The electric and magnetic boundary conditions for p-polarised waves are equally given by

$$E_{I,p} \cos \theta_1 - E_{R,p} \cos \theta_1 = E_{T,p} \cos \theta_2 \quad \text{and} \quad H_{I,p} + H_{R,p} = H_{T,p}. \quad (2.40)$$

The magnetic boundary condition is again rewritten in terms of the electric field, i.e.

$$n_1(E_{I,p} + E_{R,p}) = n_2 E_{T,p}. \quad (2.41)$$

The Fresnel equations for the p-polarisation are then expressed as

$$r_p = \frac{n_2 \cos \theta_1 - n_1 \cos \theta_2}{n_2 \cos \theta_1 + n_1 \cos \theta_2} \quad \text{and} \quad t_p = \frac{2n_1 \cos \theta_1}{n_2 \cos \theta_1 + n_1 \cos \theta_2}. \quad (2.42)$$

The ratio of reflected to incident radiant power  $R$  is called reflectance, whereas the ratio of transmitted to incident radiant power  $T$  is transmittance. The radiant power is given by the Poynting vector  $\vec{S}$ , which points in the direction of the wave vector  $\vec{k}$ , and the power striking the interface is the normal component

$$\langle \vec{S} \rangle \cdot \vec{e}_z \propto |\vec{E}|^2 \vec{e}_k \cdot \vec{e}_z = |\vec{E}|^2 \cos \theta. \quad (2.43)$$

Since  $\theta_I = \theta_R$  the reflectance and transmittance are given as

$$R = \frac{|E_R|^2}{|E_I|^2} \quad \text{and} \quad T = \frac{n_2 \cos \theta_2 |E_T|^2}{n_1 \cos \theta_1 |E_I|^2}. \quad (2.44)$$

## 2.2 Terahertz Time-Domain Spectroscopy

THz time-domain spectroscopy is utilised to obtain information about the optical properties of materials or systems in the frequency range of roughly 0.1 to 5 THz by coherent subpicosecond electromagnetic pulses. Figure 2.3 illustrates a typical linear THz time-

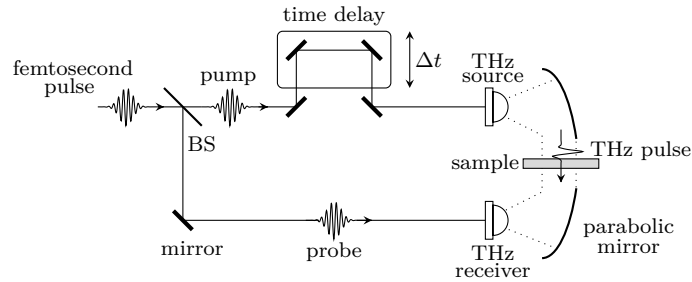


**Figure 2.3:** Illustrative scheme of a basic linear terahertz time-domain spectrometer utilising the pump-probe technique.

domain spectrometer pumped by a femtosecond laser. The optical beam of femtosecond pulses is divided into a pump and a probe branch by a 50/50 beamsplitter (BS). The pump-probe technique is applied to implement a temporal reference frame by a relative time delay  $\Delta t$  between the pump since no absolute time reference exists. In either of the two branches the time delay is scanned by a mechanical translation stage controlled by a computer, which changes the optical path length of the pulses. The pulses of the pump branch are focused on the THz source (emitter), where transients generate one to two picosecond coherent single-cycle electrical pulses. Due to the very short pulse width of the generated pulses the frequency spectrum ranges over a few THz. The generated

## 2.2. Terahertz Time-Domain Spectroscopy

THz pulse propagates from the THz source through free-space and eventually a sample before arriving at the THz receiver (detector), at which the optical pulses of the probe branch are focused. The THz field induces transient currents in the detector proportional to the electric field measured by an ammeter. Since the detector signal is proportional to the electric field, the measurements are phase sensitive implying that the absorption coefficient and the index of refraction can be determined simultaneously without solving the Kramers-Kronig relations. This is a clear advantage of THz-TDS compared to other techniques. The response currents of the detector are usually in the range of hundreds of picoamperes to a few nanoamperes. Therefore, to improve the signal-to-noise ratio a lock-in amplifier is used to measure the current. To apply the lock-in measurement technique a reference modulation of the generated THz signal is required. Often a reference frequency is introduced by either a rotational optical chopper positioned either right before or after the emitter or by a function generator depending on the THz source and receiver.

In THz-TDS, measurements are made with and without the sample of interest. Measurement without the sample serves as a reference such that a transmission coefficient containing the change in both the amplitude and the phase due to the sample is acquired. The dispersion of the sample is achieved by Fourier transforming the time-domain data into the frequency-domain.

The THz source and the THz receiver can rely on different techniques such as photoconductive switching or nonlinear effects. The spectrometer utilised in this project is based on photoconductive antennas, and hence, only this technique is examined in the subsequent sections preceding a discussion of how to analyse the data.

### 2.2.1 Photoconductive Generation of Broadband Terahertz Pulses

THz pulses are generated by an ultrafast change in polarisation caused by short femtosecond laser pulses, which can be done by various techniques. The oldest but yet very common technique in THz spectroscopy and imaging due to the operation at room temperature and ability to produce broadband THz pulses, among other things, is based on photoconductive antennas. This approach utilises a biased photo switch being a semicon-

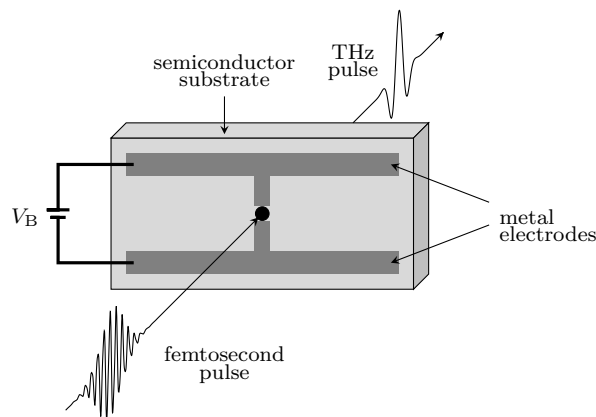


**Figure 2.4:** Illustration of THz pulse generation from a biased photoconductive antenna. Femtosecond laser pulses are focused in the gap to excite photocarriers.

ductor substrate with on top two metal electrodes often of gold or aluminum deposited. The photoconductive generation of THz pulses is illustrated in Figure 2.4. A photo switch rely on photoconductivity, i.e. the ability of semiconductors and isolators to increase electric conductivity when light is incident upon them generating electron-hole pairs and as

a result increases the density of free carriers. Thus, the photoconductive effect requires a match between the incident photon energy and the semiconductor substrate bandgap. Because of the wide usage of Ti:sapphire femtosecond lasers, such as gallium arsenide (GaAs) and indium GaAs (InGaAs) are common substrate materials. The substrate of choice in telecom systems is often InGaAs. Femtosecond laser pulses are focused between the electrodes shorting the switch electrically. Clearly, the switch-on and off times depends on the pulse duration and the lifetime of the excited photocarriers, respectively. Both generation and detection of THz radiation imply rapid changes of the induced polarisation of the substrate, obviously relating to the switching times. Hence, short lifetimes are essential, but other properties such as high carrier mobility and high breakdown voltage are favourable. Therefore, photoconductive antennas designed for 800 nm femtosecond laser pulses are most often based on Low-temperature grown gallium arsenide (LT-GaAs) with carrier lifetime in the subpicosecond range. The very short lifetime of the photocarriers is attained from a high defect concentration, where electron-hole pairs are trapped and recombined. The defect concentration is controlled by the exact growth of the LT-GaAs. Molecular beam epitaxy at low temperatures followed by rapid thermal annealing is used to grown the LT-GaAs substrate. This produces arsenide antisites and interstitials and gallium related vacancies, which accordingly result in a high density of point defects lowering the carrier lifetime down to  $\sim 0.2$  ps. The effective carrier mobility of LT-GaAs ranges from 200 to 400  $\text{cm}^2/\text{V}\cdot\text{s}$  being one order of magnitude larger than the hole mobility in the THz frequency range, hence, the carrier transport is dominated by electrons.[2] The metal electrodes of the photoconductive antennas are commonly biased with a voltage of 10 to 50 V, either DC in the simplest case or AC depending on the setup, and the antenna geometry can vary from simple strip lines through an H-like dipole structure to more complex geometries such as bow-tie or log-spiral antennas from microwave theory. In any case, the optical femtosecond pulses are focused in the photoconductive gap of the biased antenna electrodes typically in the order of 5 to 100  $\mu\text{m}$ . Consequently, photocarriers are excited and accelerated by the bias inducing a current between the electrodes. The excited carriers are then trapped by defects in the semiconductor on the time scale of the carrier lifetime, thereby decreasing the charge density. The instant generation of current paired with the rapid decay of the free carriers induce an ultrafast change in polarisation, and thus, radiates a subpicosecond, single-cycle coherent electromagnetic pulse polarised in the direction of the bias field. To understand the generation of THz pulses from bi-

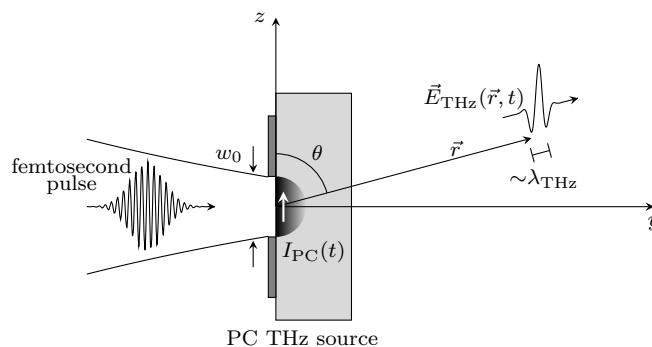


**Figure 2.5:** Illustration of the Hertzian dipole model of the radiation source in a PC antenna.

ased photoconductive antennas better, a simple model is sought. For this model an H-like dipole geometry with a DC bias is considered with a photoconductive gap comparable to the spotsizes of the focused laser beam  $w_0 \sim 10 \mu\text{m}$ . Since the size of the radiation source

## 2.2. Terahertz Time-Domain Spectroscopy

is much smaller than the THz wavelength  $\lambda_{\text{THz}}$  a Hertzian dipole antenna of size much smaller than the emitted wavelength can be considered. Therefore, a dipole approximation is reasonable. The model can be simplified a bit further since only the far-field range  $r \gg \lambda_{\text{THz}}$  is of interest. Furthermore, free space dipole radiation is assumed to simplify matters additionally. A schematic illustration of the model is found in Figure 2.5.

Such a model was treated exhaustively in the previous ninth semester project, and therefore only the main results will be summarised. For the in-depth mathematical treatment see [1].

From classical electromagnetism the expression of a radiating dipole in free space is

$$\vec{E}(\vec{r}, t) = -\frac{k^2 p(t_r)}{4\pi\epsilon_0 r} \sin\theta \vec{e}_\theta, \quad (2.45)$$

where  $\vec{r}$  is the position vector relative to the source,  $r = |\vec{r}|$  and  $\theta$  the radial and azimuthal coordinates of the position vector,  $\vec{e}_\theta$  the unit vector in the direction of  $\theta$ . The retarded time is  $t_r = t - r/c$ , and  $c$  is the speed of light in free space,  $p(t) = p_0 e^{-i\omega t}$  the time-dependent oscillating dipole moment.  $k = |\vec{k}|$  is the ordinary wave number and  $\epsilon_0$  the vacuum permittivity. This expression is easily rewritten as

$$\vec{E}_{\text{THz}}(\vec{r}, t) = \frac{\mu_0 \sin\theta}{4\pi r} \frac{d^2}{dt_r^2} [p(t_r)] \vec{e}_\theta, \quad (2.46)$$

where  $\mu_0$  is the vacuum permeability, utilising the expression of the dipole moment and a little algebra.

The temporal derivative of the dipole moment is found to be the product of the optical spot size at the antenna and the time-dependent photocurrent

$$\frac{d\vec{p}(t)}{dt} = w_0 I_{\text{PC}}(t) \quad (2.47)$$

after thorough mathematical calculations and the assumption that the carrier transport between the electrodes is one dimensional such that the photocurrent only depends on time;  $I_{\text{PC}}(t)$ . Thus, combining this result with Eq. (2.46) one arrives at the remarkable result that the THz field is proportional to the time derivative of the photocurrent in the photoconductive gap of the antenna

$$\vec{E}_{\text{THz}}(\vec{r}, t) \propto \frac{d}{dt_r} [I_{\text{PC}}(t_r)]. \quad (2.48)$$

The time-dependent photocurrent can be expressed as the convolution of the optical pulse envelope and the impulse response of the photocurrent [2]

$$I_{\text{PC}}(t) = \int I_{\text{opt}}(t - t') [e n_c(t') v(t')] dt'. \quad (2.49)$$

Here  $I_{\text{opt}}$  is the intensity profile of the optical pulses,  $e$  the electron charge,  $n_c(t)$  the carrier density, and  $v(t)$  the average electron velocity. In this expression the holes are ignored as charge carriers, since the hole mobility in common photoconductive substrates is negligible compared to the electron mobility. The carrier transport of the excited electrons is well-described by the Drude-Lorentz model, i.e. the dynamics of the carrier density follow

$$\frac{dn_c(t)}{dt} = -\frac{n_c(t)}{\tau_c} + \delta(t) \quad \text{with} \quad n_c(t) = \begin{cases} e^{-t/\tau_c} & \text{for } t > 0 \\ 0 & \text{for } t < 0 \end{cases}. \quad (2.50)$$

Here  $\tau_c$  is the carrier lifetime and the Dirac delta function accounts for the spontaneous optical excitation. According to the Drude-Lorentz model the average velocity obeys

$$\frac{dv(t)}{dt} = -\frac{v(t)}{\tau_s} + \frac{e}{m}E_{\text{DC}}\theta(t), \quad \text{with} \quad v(t) = \begin{cases} \mu_e E_{\text{DC}}(1 - e^{-t/\tau_s}) & \text{for } t > 0 \\ 0 & \text{for } t < 0 \end{cases}. \quad (2.51)$$

The Heaviside step function [7]

$$\theta(t) = \begin{cases} 1 & \text{for } t > 0 \\ 0 & \text{for } t < 0 \end{cases} \quad (2.52)$$

accounts for the impulsive excitation and  $\tau_s$  is the carrier collision time,  $m$  is the effective carrier mass,  $E_{\text{DC}}$  is the applied DC bias field, and  $\mu_e = e\tau_s/m$ . In this model the electrostatic screening effect triggered by the space-charge field of the electron-hole pairs is omitted. This is reasonable as long as the carrier density is small enough to satisfy  $\omega_p\tau_s \ll 1$  with the plasma frequency  $\omega_p^2 = n_c e^2 / \varepsilon_0 m$  since the screening field is then much smaller than the bias field [8]. Note that the condition  $\omega_p\tau_s > 0$  given in [2] is inadequate.

The optical pulses are assumed to be Gaussian

$$E(t) = E_0 e^{a_0 t^2} e^{-i\omega_0 t}, \quad (2.53)$$

such that the instantaneous intensity in a linear medium of refractive index  $n$  is

$$I(t) = \frac{1}{2} \varepsilon_0 c n E_0^2 e^{-2a_0 t^2}. \quad (2.54)$$

The full-width at half-maximum (FWHM) pulse duration is given as

$$\tilde{\tau}_p = \sqrt{2 \ln 2 / a_0}. \quad (2.55)$$

If this be equal to  $2\sqrt{\ln 2} \cdot \tau_p$ , such that  $a_0 = 1/2\tau_p^2$ , the optical intensity profile becomes

$$I_{\text{opt}}(t - t') = I_{\text{opt}0} e^{-(t-t')^2/\tau_p^2} \quad \text{with} \quad I_{\text{opt}0} = \frac{1}{2} \varepsilon_0 c n E_0^2 \quad (2.56)$$

and the photocurrent can be treated analytically. When the calculations are carefully done one arrives at the result

$$I_{\text{PC}}(t) = \frac{\sqrt{\pi}}{2} e \mu_e \tau_p I_{\text{opt}0} E_{\text{DC}} \left\{ \exp \left[ \frac{\tau_p^2}{4\tau_c^2} - \frac{t}{\tau_c} \right] \text{erfc} \left( \frac{\tau_p}{2\tau_c} - \frac{t}{\tau_p} \right) - \exp \left[ \frac{\tau_p^2}{4\tau_{cs}^2} - \frac{t}{\tau_{cs}} \right] \text{erfc} \left( \frac{\tau_p}{2\tau_{cs}} - \frac{t}{\tau_p} \right) \right\}. \quad (2.57)$$

The photocurrent and the coupled THz far field of carrier lifetime  $\tau_c = 0.5$  ps, carrier collision time  $\tau_s = 0.03$  ps, and optical pulse duration  $\tau_p = 0.048$  ps are computed in Figure 2.6. Evidently, the rising edge of the photocurrent is much faster than the longer decaying tail due to the carrier lifetime. This translates directly to the THz pulse due to the temporal derivative of the transient photocurrent. Thus, the long tail has no distinct effect on the radiated THz field.

The antenna design and in particular the electrode geometry include important parameters that affect both the bandwidth and the radiated power directly. If Eq. (2.57) is considered this is easily seen as the photocurrent depends on the bias voltage and the optical pump

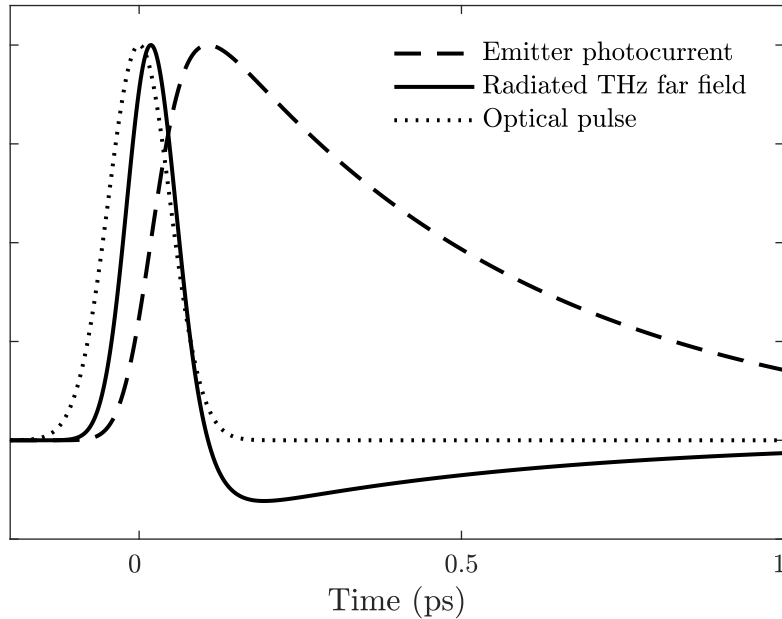


**Figure 2.6:** Computed photocurrent (dashed line) in a photoconductive THz source and the coupled THz far field radiation amplitude (solid line). The temporal shape of the optical femtosecond pulses are also shown (dotted line). Typical substrate and physical parameters  $\tau_c = 0.5$  ps,  $\tau_s = 0.03$  ps, and  $\tau_p = 0.048$  ps have been applied in the calculations.

power, and since Eq. (2.48) dictates that the radiated THz field is proportional to the time derivative of the photocurrent, the amplitude of the generated field increases linearly with both. However, when the optical power is increased sufficiently photocarriers screen the bias field, and thus, saturating the field amplitude. Typically, stripline antennas are designed with an electrode separation of 30-100  $\mu\text{m}$  while dipole antenna geometries have dipole gaps of 5-10  $\mu\text{m}$ . Due to this smaller dimension of the active area dipole antennas will saturate faster than other antenna designs.

A crucial fact to remember is that this approximation assumes a dipole in free-space disregarding the dielectric air-substrate interface. The substrate is typically GaAs with dielectric constant  $\epsilon_r \approx 12$  in which the photocurrent flows and the pulses are generated, wherefore a considerable portion of the THz field propagates into the substrate. The generated THz radiation is also highly divergent due to the very small size of the source compared to the terahertz wavelength  $\lambda_{\text{THz}}$ . Hence, the actual radiation pattern is much more complicated than the free-space dipole pattern and to collimate and couple the THz radiation out from the source a substrate lens is necessary. Commonly, high resistivity silicon (HR-Si) is used when such lenses are fabricated due to very low linear absorption and negligible dispersion at THz frequencies, a good match of refractive index with common photoconductive substrate materials, and the ability without difficulties to fabricate high-quality components. However, a theoretical treatment of substrate lenses is omitted in this project.

### 2.2.2 Photoconductive Detection of Broadband Terahertz Pulses

Photoconductive antennas can also be used to detect broadband terahertz pulses and the detection mechanisms are very similar to the mechanisms of generation. The situation of a photoconductive antenna driven as a THz receiver is illustrated in Figure 2.7. The

electrodes of a photoconductive THz receiver are not biased as they are in the case of a photoconductive THz source. An optical pump of femtosecond pulses is again focused on the antenna to excite free carriers in the photoconductive gap which are accelerated by the incoming THz electric field. Hence, a photocurrent flows between the two electrodes which can be measured by an ammeter. The duration of the photocurrent is governed by the carrier lifetime. Hence, the carrier lifetime should be much shorter than the THz pulse in time-resolved pulse shape measurements. Recall that the THz field strength is proportional to the temporal derivative of the photocurrent. In consequence, the THz pulse shape can be mapped in the time-domain through the photocurrent if the time delay between the optical probe pulse and the THz pulse is scanned. The photocurrent, however, is in the subnanoamps range, and therefore a current amplifier is required and in most cases a lock-in amplifier is used to increase the signal-to-noise ratio.

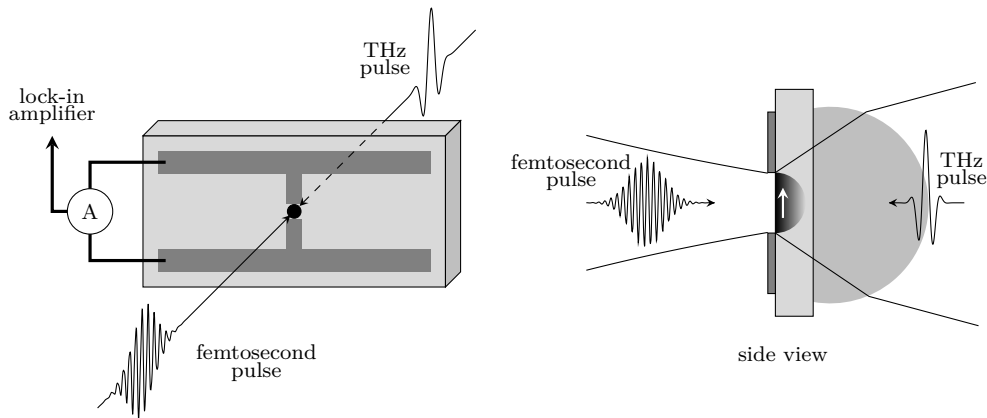


**Figure 2.7:** Illustration of THz pulse detection utilizing a photoconductive antenna.

As in the previous section a full mathematical treatment of the following model was made in my ninth semester project [1] last semester, hence, only the main results will be given here. The photocurrent generated by the THz field to be measured depends on the transient surface conductivity

$$\sigma_s(t) = \frac{e(1 - R_{\text{opt}})}{\hbar\omega} \int_{-\infty}^t I_{\text{opt}}(t') \mu(t, t') n(t, t') dt' \quad (2.58)$$

with electron charge  $e$ , optical reflectivity of the photoconductor  $R_{\text{opt}}$ , and photon energy  $\hbar\omega$ . The mobility at time  $t$  of a photoexcited electron created at time  $t'$  is denoted  $\mu(t, t')$  and the population of electrons at time  $t$  created at  $t'$  is denoted  $n(t, t')$ . [2]

This means that the measured photocurrent is a convolution of the field strength and the conductivity

$$j(t) = \int_{-\infty}^t \sigma_s(t - t') E_{\text{THz}}(t') dt' \quad (2.59)$$

implying that the photocurrent in the detector is not generated instantaneously because of the time-dependency of earlier times  $t'$  of the THz field. Clearly, this convolution only equals the genuine THz waveform  $j(t) = E(t)$  if  $\sigma_s(t)$  is a delta function, hence, materials with ultrashort lifetime smaller than 0.5 ps is preferable. However, it is also possible to have photoconductive THz receivers with very long carrier lifetimes and short carrier density risetimes such that the conductivity can be treated as the Heaviside step function

[8]. The Heaviside step function  $\theta(t - t')$  is equal to one within the integration interval of (2.59)

$$j(t) = \int_{-\infty}^t E_{THz}(t') dt', \quad (2.60)$$

i.e the measured current is the temporal integrated field of the THz pulse. Thus, the photoconductive antenna functions as an integrator if lifetime is long and the risetime of the carrier density is short.

The frequency-dependent photocurrent

$$j(\nu) = \sigma(\nu)E_{THz}(\nu) \quad (2.61)$$

simply follows as product of the Fourier transform of the conductivity and the THz electric field according to the convolution theorem [9]. Notice how the conductivity acts as a frequency filter, and thus, how the photocurrent not replicates the THz pulse shape exactly and that the carrier dynamics of the photoconductive substrate limits the detection bandwidth.

The surface conductivity is related to the optical intensity, the carrier drift velocity, and the carrier population, however, in the previous section the optical intensity was assumed to be Gaussian

$$I_{opt}(t) = I_0 e^{-t^2/\tau_p^2} \quad (2.62)$$

while the carrier drift due to a bias field

$$\mu(t, t') = \mu_e \left(1 - e^{-(t-t')/\tau_s}\right), \quad (2.63)$$

where  $\mu_e$  is the electron mobility for stationary charge transport and  $\tau_s$  is the momentum relaxation time, and the electron population

$$n(t, t') = e^{-(t-t')/\tau_c} \quad (2.64)$$

with carrier lifetime  $\tau_c$  was derived from the Drude-Lorentz model. These expressions allow the conductivity to be calculated analytically for ultrashort carrier lifetimes and the result is

$$\sigma_s(t) = \sigma_0 \left\{ \exp \left[ -\frac{t}{\tau_c} + \frac{\tau_p^2}{4\tau_c^2} \right] \left( 1 + \operatorname{erf} \left( \frac{t}{\tau_p} - \frac{\tau_p}{2\tau_c} \right) \right) - \exp \left[ -\frac{t}{\tau_{cs}} + \frac{\tau_p^2}{4\tau_{cs}^2} \right] \left( 1 + \operatorname{erf} \left( \frac{t}{\tau_p} - \frac{\tau_p}{2\tau_{cs}} \right) \right) \right\}, \quad (2.65)$$

where  $1/\tau_{cs} = 1/\tau_c + 1/\tau_s$ . In Figure 2.8 the surface conductivity  $\sigma_s(t)$  and the amplitude of its Fourier transform  $\sigma_s(\omega)$  is computed using the same parameters as when the photocurrent in the THz source was computed above; carrier collision time  $\tau_s = 0.03$  ps, carrier lifetime  $\tau_c = 0.5$  ps, and optical pulse width  $\tau_p = 0.048$  ps. The Fourier spectrum of the modelled detector reveals that frequencies up to  $\sim 4$  THz can be measured. However, it has been shown in [8] that the spot size of the THz beam depends on frequency which limits the responsivity of the detector due to diffraction resulting in a weaker field strength at the detector at low frequencies. The response function of the detector is proportional to the frequency in low frequency range and is shown in Figure 2.8 by the dashed line.

Recently it was reported by T.K. Nguyen et al. in [10] that I-shaped and bowtie antennas produce detection peaks around 0.2 THz compared to 0.8 THz of H-shaped antennas. It

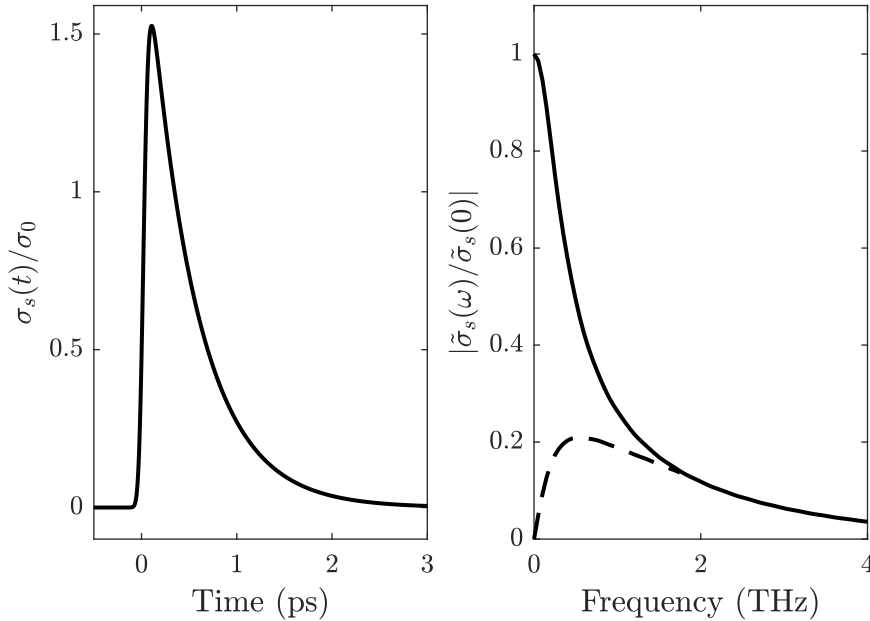


**Figure 2.8:** The surface conductivity  $\sigma_s(t)$  and the amplitude of its Fourier transform  $\sigma_s(\omega)$  computed using the parameters carrier collision time  $\tau_s = 0.03$  ps, carrier lifetime  $\tau_c = 0.5$  ps, and optical pulse width  $\tau_p = 0.048$  ps. The dashed line indicates the response function due to diffraction.

is found that I-shaped and bow-tie antennas are much more sensitive below 0.6 THz than H-shaped antennas. Furthermore, T.K. Nguyen et al. find that there is a lower limit of the detection bandwidth using PCAs on GaAs around 0.2 THz, possibly due to the spectral convolution of the responses of the photoconductive substrate and the antenna, including the geometry and the substrate lens.

### 2.2.3 Data Analysis in Terahertz Transmission Spectroscopy

The signal measured in THz-TDS is proportional to the electric field of the THz pulse  $E(t)$  revealing both the amplitude and the phase. The spectral amplitude and phase of the measured pulse can be accessed by Fourier transforming the signal

$$E(\omega) = \frac{1}{2\pi} \int_{-\infty}^{\infty} E(t) e^{-i\omega t} dt. \quad (2.66)$$

In transmission spectroscopy both a scan where the pulse propagates through the sample of interest and a scan without the sample acting as a reference are recorded. These two traces are denoted  $E_s$  and  $E_r$ , respectively, and from these it is possible to determine the optical properties of the sample such as the real and imaginary part of the dielectric function  $\varepsilon(\omega) = [\tilde{n}(\omega)]^2$ , where  $\tilde{n}(\omega) = n(\omega) + i\kappa(\omega)$  is the complex refractive index, or the real refractive index  $n(\omega)$  and the absorption coefficient  $\alpha(\omega) = 2\kappa(\omega)\omega/c$ . In Figure 2.9 the geometry for transmission measurements is illustrated. The sample generally has a known well-defined thickness  $d$  and the surfaces are smooth and parallel.

The incident THz pulse  $E_0(\omega)$  interacts with the layer and parts of the field are reflected multiple times at the interfaces before they're transmitted through. As the field propagates within the layer the phase is shifted by

$$\exp[i\varphi_{\text{sam}}(\omega, d)] \quad \text{with} \quad \varphi_{\text{sam}}(\omega, d) = \tilde{n}(\omega) \frac{\omega d}{c}. \quad (2.67)$$

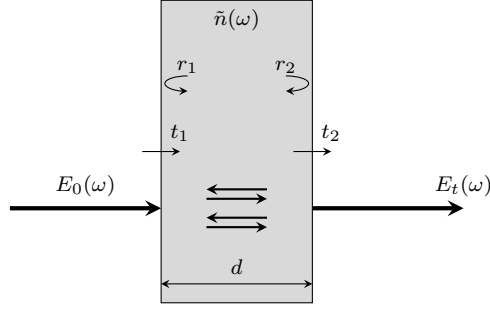


**Figure 2.9:** Schematic illustration of the geometry for transmission spectroscopy.  $E_0(\omega)$  is the field incident on a single flat layer of material with complex refractive index  $\tilde{n}(\omega)$  and thickness  $d$ . The reflection and transmission coefficients at the entrance and exit surfaces are denoted  $r_1$ ,  $r_2$  and  $t_1$ ,  $t_2$ , respectively.  $E_t(\omega)$  is the transmitted field.

Given normal incidence and planar surfaces without scattering the Fresnel equations derived above holds and with the assumption that the surrounding medium is dry air the complex refractive index can be set to 1, thus,

$$r_1(\omega) = r_2(\omega) = \frac{\tilde{n}(\omega) - 1}{\tilde{n}(\omega) + 1}, \quad t_1(\omega) = \frac{2}{\tilde{n}(\omega) + 1}, \quad \text{and} \quad t_2(\omega) = \frac{2\tilde{n}(\omega)}{\tilde{n}(\omega) + 1}. \quad (2.68)$$

However, the model still holds when the surrounding medium is ambient air as long as the absorption lines of the water vapor do not obscure the frequency range of interest, since the absorption due to water vapor will occur in both the reference and the sample measurement.

The field transmitted through the sample can then be expressed as a superposition of the multiple reflections

$$E_{\text{sam}} = E_0 t_1 t_2 e^{i\varphi_{\text{sam}}} \sum_{m=0}^{\infty} (r_1 r_2 e^{i2\varphi_{\text{sam}}})^m = \frac{E_0 t_1 t_2 e^{i\varphi_{\text{sam}}}}{1 - r_1 r_2 e^{i2\varphi_{\text{sam}}}}, \quad (2.69)$$

where the identity of a geometric series has been applied.

The reference pulse does not experience any reflections and acquires only a phaseshift

$$\varphi_{\text{ref}}(\omega, d) = \frac{\omega d}{c} \quad (2.70)$$

as it propagates a distance  $d$  through air, hence,

$$E_{\text{ref}} = E_0 e^{i\varphi_{\text{ref}}}. \quad (2.71)$$

The transfer function  $H(\omega)$  is defined as the ratio of the transmitted and the reference field [4]

$$H(\omega, \tilde{n}) \equiv \frac{E_{\text{sam}}}{E_{\text{ref}}} = \frac{4\tilde{n}(\omega)}{(\tilde{n}(\omega) + 1)^2 - (\tilde{n}(\omega) - 1)^2 \exp\left[i2\tilde{n}(\omega)\frac{\omega d}{c}\right]} \exp\left[i(\tilde{n}(\omega) - 1)\frac{\omega d}{c}\right]. \quad (2.72)$$

This is a function of the complex refractive index  $\tilde{n}(\omega)$ , thus, this has to be varied in order to fit the experimental transfer function, and when the two transfer functions  $H_{\text{model}}$  and

$H_{\text{experiment}}$  are equalised the refractive index of the sample material is found at the given frequency. If a function  $f$  is defined as

$$f(\omega, \tilde{n}) = H_{\text{model}}(\omega, \tilde{n}) - H_{\text{experiment}}(\omega, \tilde{n}), \quad (2.73)$$

then the refractive index of the sample is found at the given frequency when  $f(\omega, \tilde{n}) = 0$ . The iterative Newton-Raphson method is clearly qualified to carry out the fitting process [4; 11]. For each frequency component  $\omega_i$  an initial guess  $\tilde{n}_0$  is made. Next, the function  $f(\omega_i, \tilde{n})$  is expanded as a Taylor series in  $\tilde{n} - \tilde{n}_0$

$$f(\omega_i, \tilde{n}) = f(\omega_i, \tilde{n}_0) + f'(\omega_i, \tilde{n}_0)(\tilde{n} - \tilde{n}_0) + \frac{1}{2}f''(\omega_i, \tilde{n}_0)(\tilde{n} - \tilde{n}_0)^2 + \dots \quad (2.74)$$

where  $f'(\omega_i, \tilde{n})$  denotes the first derivative of  $f(\omega_i, \tilde{n})$  with respect to  $\tilde{n}$ , etc. Provided that  $\tilde{n}_0$  is close to the true root,  $\tilde{n} - \tilde{n}_0$  is small and only the first terms in the expansion are important to get an accurate estimate of the true root

$$0 = f(\omega_i, \tilde{n}) \approx f(\omega_i, \tilde{n}_0) + f'(\omega_i, \tilde{n}_0)(\tilde{n} - \tilde{n}_0). \quad (2.75)$$

This gives the Newton-Raphson iteration formula for a better estimate of the true root

$$\tilde{n}_1 = \tilde{n}_0 - \frac{f(\omega_i, \tilde{n}_0)}{f'(\omega_i, \tilde{n}_0)}. \quad (2.76)$$

Thus, the Newton-Raphson method finds the tangent of  $f(\omega_i, \tilde{n})$  at  $\tilde{n} = \tilde{n}_0$  and extrapolates it to the intersection of the  $\tilde{n}$ -axis ( $\tilde{n}_1, 0$ ) to find a new estimate  $\tilde{n}_1$  of the true root. The procedure is repeated until it converges. Given the value  $\tilde{n} = \tilde{n}_x$  at the end of the  $x$ th iteration

$$\tilde{n}_{x+1} = \tilde{n}_x - \frac{f(\tilde{n}_x)}{f'(\tilde{n}_x)} \quad (2.77)$$

is obtained. The function  $f$  may be more conveniently defined as the natural logarithm of the transfer functions to circumvent the need of phase unwrapping [4].

The method for refractive index extraction can be simplified by neglecting the etalon effect, i.e. the echoes of the THz pulse due to multiple reflections within the sample. This is acceptable if the sample is thick and the echoes are avoided by truncating the recorded data. In thin samples with a strong etalon effect the accuracy is thus limited by this method [4]. Neglecting the etalon effect the transfer function becomes

$$H(\omega, \tilde{n}) = \frac{4\tilde{n}(\omega)}{(\tilde{n}(\omega) + 1)^2} \exp \left[ i(\tilde{n}(\omega) - 1) \frac{\omega d}{c} \right]. \quad (2.78)$$

Considering only materials with low absorption coefficient  $\alpha(\omega) = 2\kappa(\omega)\omega/c$  imply real-valued Fresnel transmission coefficients [12]

$$t_1(\omega) = \frac{2}{n(\omega) + 1}, \quad \text{and} \quad t_2(\omega) = \frac{2n(\omega)}{n(\omega) + 1}, \quad (2.79)$$

hence,

$$H(\omega, n) = \frac{4n(\omega)}{(n(\omega) + 1)^2} \exp \left[ i(n(\omega) - 1) \frac{\omega d}{c} \right] \exp \left[ -\frac{1}{2}\alpha(\omega)d \right]. \quad (2.80)$$

The transfer function of the measured data is a complex number of amplitude  $R$  and phase  $\Phi$  that can be written as

$$H(\omega) = R(\omega)e^{i\Phi(\omega)}. \quad (2.81)$$

Therefore, by solving the equation

$$H_{\text{experiment}}(\omega) = H_{\text{model}}(\omega) \quad (2.82)$$

analytic expressions for the refractive index and the absorption coefficient is found

$$n(\omega) = 1 + \frac{c}{\omega d} \Phi(\omega), \quad (2.83)$$

$$\alpha(\omega) = -\frac{2}{d} \ln \left[ \frac{(n(\omega) + 1)^2}{4n} R(\omega) \right]. \quad (2.84)$$

Finally, the complex refractive index can be computed as

$$\tilde{n}(\omega) = n(\omega) + i\kappa(\omega) \quad \text{with} \quad \kappa(\omega) = \frac{c}{2\omega} \alpha(\omega) \quad (2.85)$$

before the complex relative dielectric function can be determined

$$\varepsilon_r(\omega) = [\tilde{n}(\omega)]^2 = \varepsilon_{r1}(\omega) + i\varepsilon_{r2}(\omega). \quad (2.86)$$

In order to calculate the real part of the refractive index in Eq. (2.83) and the absorption coefficient in Eq. (2.84) the transmission phase  $\Phi(\omega)$  from the experimental data is required. The phase information is nothing but the complex argument of the transfer function  $H(\omega)$ , thus,

$$\Phi(\omega) = \arg(H(\omega)) = \arctan \left( \frac{\text{Re}H(\omega)}{\text{Im}H(\omega)} \right). \quad (2.87)$$

MATLAB is used to handles the experimental data and the phase is simply acquired by applying the `angle()` command to the Fourier transformed data. However, since the arctan function has a periodic nature, the phase will not be continuous. To correct the jumps of  $2\pi$  the phase has to be unwrapped, which can be done in several ways but the simplest is to use the MATLAB command `unwrap()` on the extracted phase. Figure 2.10 illustrates the discontinuouness of the wrapped phase and the corrected unwrapped phase.

### Discrete Fourier Transform

In the experiment the photocurrent flowing across the detector antenna which is proportional to the electric THz field  $E(t)$  is measured by a lock-in amplifier while a time delay is varied consecutively over  $N$  equal steps, hence, the measured signal is discretely sampled at a fixed time interval  $\Delta t$  between each data sample. The sampled sequence is then

$$E_n = E(n\Delta t), \quad n = 1, 2, \dots \quad (2.88)$$

The sampling rate  $\nu_s$  is the inverse of the time interval  $\Delta t$  and for every interval  $\Delta t$  there is a Nyquist critical frequency

$$\nu_c = \frac{1}{2\Delta t}. \quad (2.89)$$

The importance of this special frequency is manifested by the sampling theorem; if a continuous function is sampled at an interval and bandwidth limited to frequencies of magnitude smaller than the Nyquist critical frequency, then the function is completely determined by its samples. This is truly a remarkable theorem but it also induces an unwanted side effect when a sampled continuous function is not bandwidth limited to less

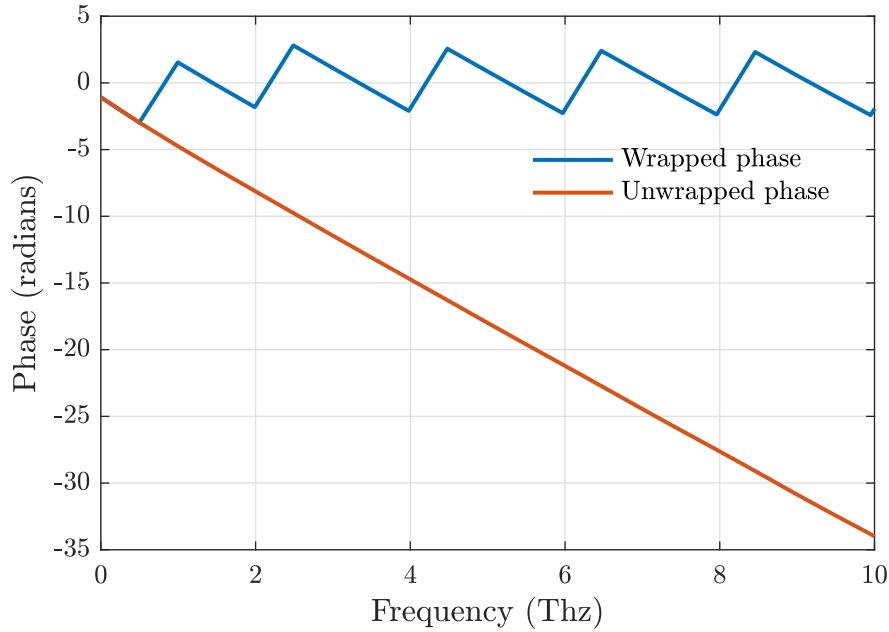


**Figure 2.10:** Illustration of the need of phase unwrapping due to the periodic nature of the arctan function.

than the Nyquist critical frequency. All of the power spectral density outside the interval  $-\nu_c < \nu < \nu_c$  is falsely translated into the interval. The effect is known as aliasing and any frequency component outside the Nyquist critical range  $(-\nu_c, \nu_c)$  is said to be aliased into the interval due to the discrete sampling. [6]

To investigate the alias phenomenon a bit further the radiated THz far field from a photoconductive antenna with substrate parameters carrier collision time  $\tau_s = 0.03$  ps, carrier lifetime  $\tau_c = 0.5$  ps, and optical pulse duration  $\tilde{\tau}_p = 0.048$  ps has been computed. The spectral amplitudes of the computed pulse sampled with four different scan resolution  $\Delta t$  and number of sampling points  $N$  is seen in Figure 2.11. The Nyquist frequency of the blue curve recorded with a scan resolution of 100 fs and 21 points is

$$\nu_c = \frac{1}{2\Delta t} = \frac{1}{2 \cdot 100\text{fs}} = 5 \text{ THz}, \quad (2.90)$$

which is also clear from the figure. Comparing the amplitude from 3 to 5 THz with the other recordings, the alias effect is clear; power above the Nyquist frequency is aliased into the Nyquist range  $(0, \nu_c)$ . The records sampled with a scan resolution of 50 and 37 fs clearly show that the aliasing effect is shifted towards 10 and 13 THz, respectively. This is as expected since a smaller scan resolution results in a higher Nyquist frequency, where the aliasing happens. The Nyquist frequency of the purple (25 ps) and green (10 ps) curve is 20 and 50 THz, respectively, and a subtle alias effect can be seen on the purple curve between 14 and 18 THz compared to the green curve. However, the minima in the same range must be considered as regular features of the THz pulse, since they still appear in the green record with a Nyquist frequency of 50 THz. Note the minimum of the yellow curve around 12 THz due to the alias effect. In an experiment such minima could be more extreme, and hence, be incorrectly attributed to absorption if not treated with care, emphasising the desire to avoid alias.

It is seen that the aliasing effect occurs whenever a signal with frequencies higher than the Nyquist frequency is converted from analog to digital, i.e. from being continuous to

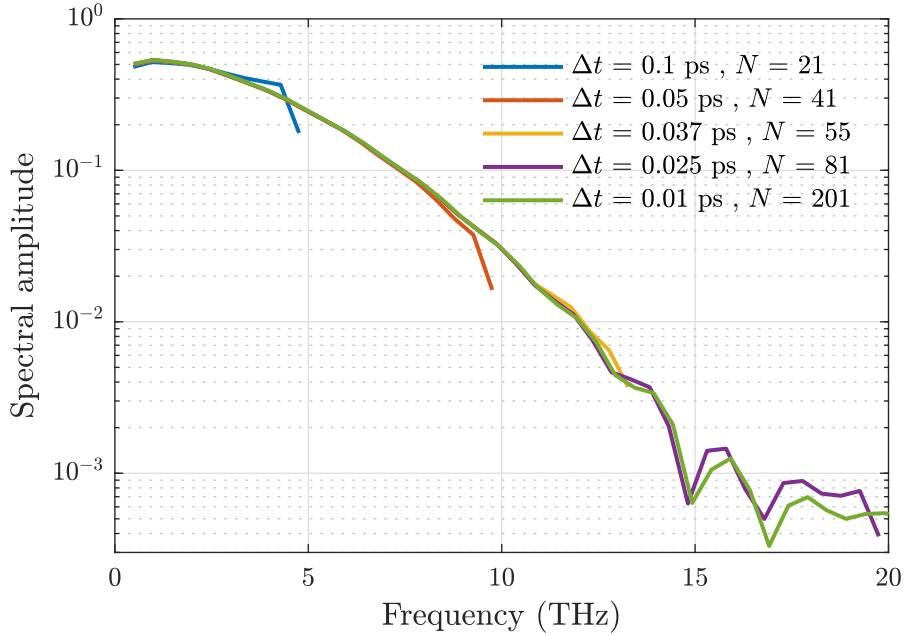


**Figure 2.11:** Spectral amplitude of a computed THz pulse sampled with different scan resolution  $\Delta t$  and number of sampling points  $N$  to illustrate and investigate the aliasing phenomenon.

discrete. In a general settings one way to avoid aliasing is to bandwidth limit the signal with an analog low-pass filter before the analog/digital conversion but this is not possible in THz-TDS, since the recorded time-domain signal in reality depend on position such that a time-based low-pass filter cannot be applied. Therefore, the only possibilities to minimise the alias effect during a THz-TDS measurement is to keep the noise level low and choose an temporal (spatial) resolution corresponding to a sampling rate least a factor of two higher than the desired THz bandwidth, i.e. a Nyquist frequency higher than the bandwidth maximum. Neither is it possible to avoid aliasing during the Fourier transformation but the effect can in some cases be moderated by padding zeros at the end of the data known as zero padding. Zero padding has other advantages, since it is well-known the Fast Fourier Transformation algorithm (FFT) used to carry out the discrete Fourier transformation (DFT) performs better when the length of the data is powers of two. This padding should not be applied without caution though.

A  $N$  point temporal signal sampled at rate  $\nu_s$  fed to the FFT represents a scan duration

$$T = N\Delta t = \frac{N}{\nu_s} \quad (2.91)$$

and the output of the FFT will be of length  $N_{\text{FFT}} = N/2 + 1$  with elements known as FFT bins ranging from 0 to  $\nu_c$ . Therefore, the resolution of the frequency components must be

$$\Delta\nu = \frac{\nu_s/2}{N/2} = \frac{1}{T}. \quad (2.92)$$

That is, the frequency resolution is inversely proportional to the time duration of the signal. When a signal is padded with  $N_z$  zeros, the FFT output has  $N_{\text{FFT}} = (N + N_z)/2 + 1$  samples while the sampling rate  $\nu_s$  is unchanged retaining the frequency span. Since the zero padded output is also evenly distributed from 0 to  $\nu_c$  the sample spacing decrease to

$$\frac{\nu_s}{N + N_z} \quad (2.93)$$

to fit the same frequency range giving a better resolution in these samples. The Fourier spectrum can be said to get a finer granularity but the frequency resolution of the analysis is not improved. As zero padding shifts the spacing of the intersamples in the frequencies problems can rise, if it alters the amplitude relative to the frequency component of interest in such a way it spreads out between the additional samples. The Fourier spectra from

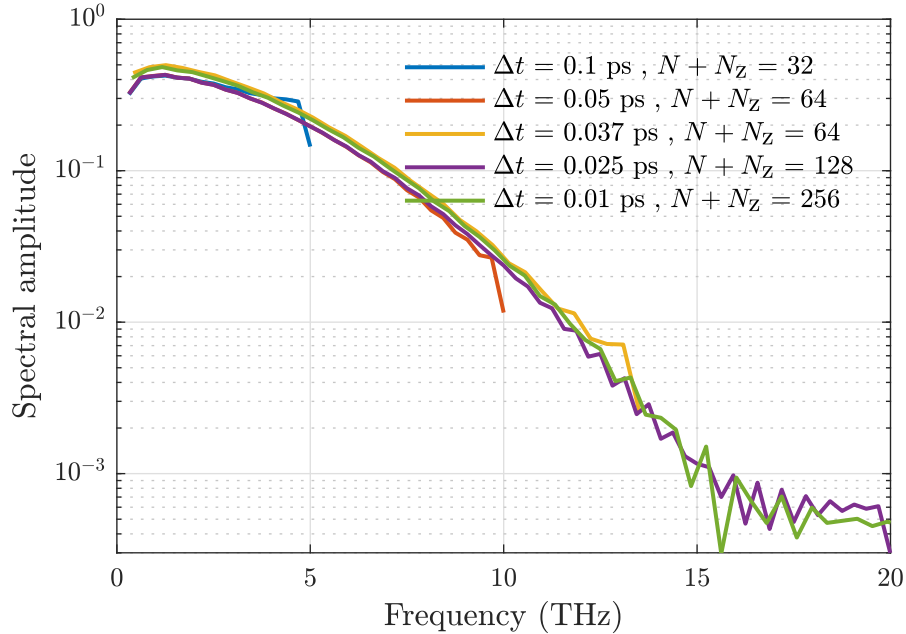


**Figure 2.12:** Spectral amplitude when zero padding to the next power of 2 of a computed THz pulse sampled with different scan resolution  $\Delta t$  and number of sampling points  $N$ .

Figure 2.11 have been recalculated with zero padding to the next power of two. The result is shown in Figure 2.12. Evidently, the aliased power of the blue, red and yellow curves is less pronounced, however, the tendency of minima due to the aliasing effect still appear. Notice how the features from 14 to 20 THz have been smeared out as a consequence of the shifted intersample spacing due to the zero padding. Furthermore, it is seen that the maximum amplitude is increased a small amount due to the zero padding. In general, the maximum amplitude scales with  $(N + N_Z)/2$  due to the padding while it scales with  $1 - (N + N_Z)/2$  if the data is truncated e.g. to the prior power of two for more efficient computations.

An interesting property that can be noticed is the relationship between the maximum of the spectral amplitude and the product of the number of samples  $N$  and the scan resolution  $\Delta t$  or simply the scan duration  $T$ . In [13] it is stated that the maximum amplitude of the Fourier transform scales with  $N\Delta t$ . This is, however, found not to be entirely correct. Figure 2.13 illustrates this relationship. The computed THz pulse is sampled with four different combinations of scan resolutions of 25 fs and 50 fs and 200 and 400 numbers of samples. When the scan duration  $T$  is equal (blue and red curve) the spectral amplitude is almost equal. The scan duration  $T$  of the yellow curve is halved compared to the blue and red curve and the result is a 41% increase in maximum amplitude, whereas a doubling of  $T$  result in a 29% decrease of the maximum amplitude, indicating that the relationship between the maximum amplitude  $M$  and the scan duration  $T$  is more likely to be inversely

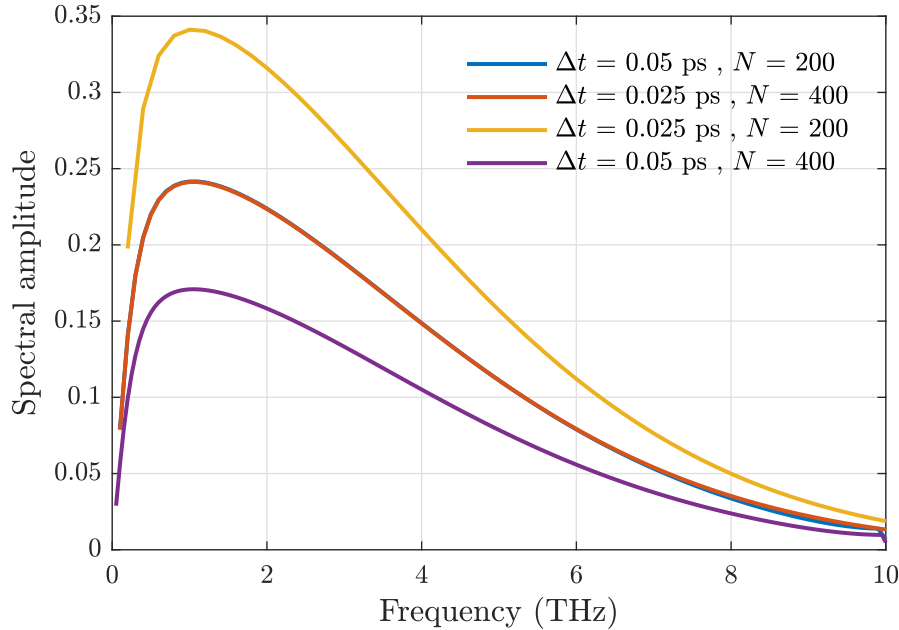


**Figure 2.13:** Spectral amplitude of a computed THz pulse with different combinations of scan resolution  $\Delta t$  and number of samples  $N$  showing the relation between the signal time duration and the maximum amplitude of the spectral amplitude.

proportional. By a little trial and error a suggestion of the scaling factor is

$$M = \sqrt{\frac{2}{\pi T}}. \quad (2.94)$$

To investigate the relation further more data is needed. In Figure 2.14 the percentage-wise deviation of the estimated maximum amplitude  $M$  in proportion to the computed amplitude is plotted for five different scan resolutions and a different number of sample points  $N$ . This shows that for scan resolutions below 50 fs the deviation settles around 4.5%. Note the blue points at 250, 300 and 350 samples, which deviates from the rest. This can be attributed to a scan duration  $T$  shorter than the actual pulse duration. This indicates that the relationship in Eq. (2.94) is partly correct as far as the  $N$  dependency if a scaling factor of 0.955 is added. Adding this factor and choosing a sufficiently large number of samples  $N = 3000$  to avoid deviations due to an inadequate scan duration  $T = N\Delta t$  the scan resolution dependency can be investigated. This is done in Figure 2.15. Below 50 fs the relation seem to be accurate, however uneven oscillations occur above 50 fs restricting the usability to  $0 < \Delta t < 50$  fs.

Figure 2.16 shows the frequency spectra of four traces of real data that is sampled with either  $\Delta t = 0.035$  ps or  $\Delta t = 0.07$  ps. The blue and the red lines both have a scan duration of nearly 17 ps while the yellow and the purple lines have a scan duration of approximately 21 ps. According to Eq. (2.94), the blue and the red lines should have an equal maximum amplitude while the yellow and the purple lines should be equal, which is clearly not the case in Figure 2.13. The real data suggest that the

$$M \propto \frac{1}{\Delta t} \quad (2.95)$$

with no dependency on  $N$ , since the peak of the red and the purple lines with  $\Delta t = 0.07$  ps are equal as are the blue and the yellow lines with  $\Delta t = 0.035$  ps.

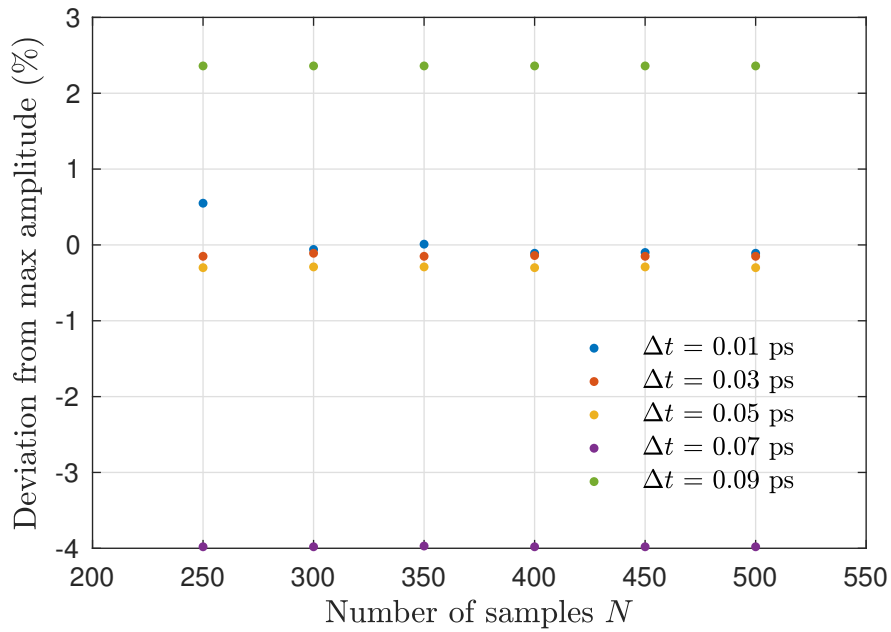


**Figure 2.14:** The percentage-wise deviation of  $M$  compared the computed amplitude as a function of number of samples  $N$  for five different scan resolutions  $\Delta t$ .

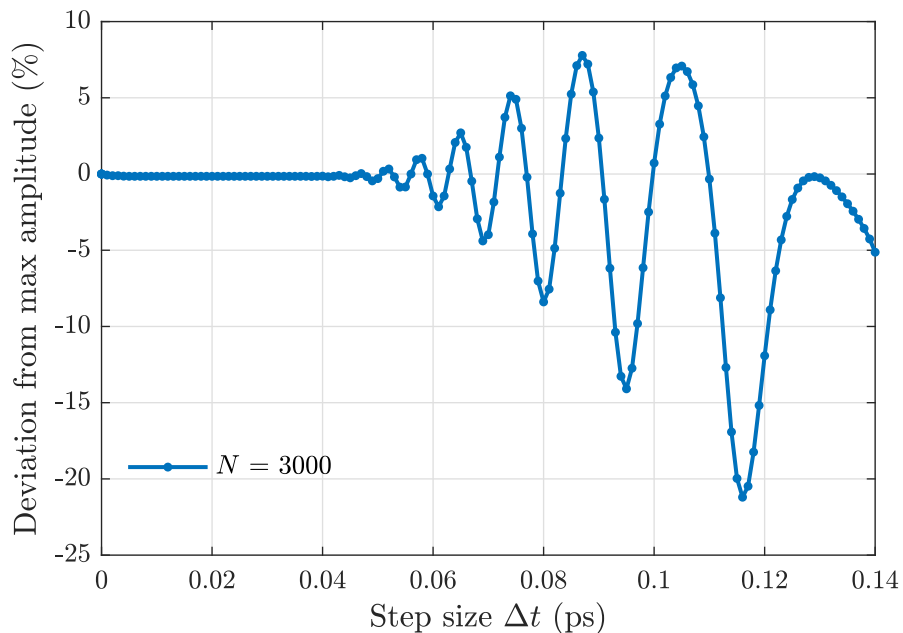


**Figure 2.15:** The percentage-wise deviation of  $0.955M$  compared to the computed amplitude as a function of the scan resolution  $\Delta t$  for a fixed number of samples  $N = 3000$ .

### 2.3. Lock-in Amplification

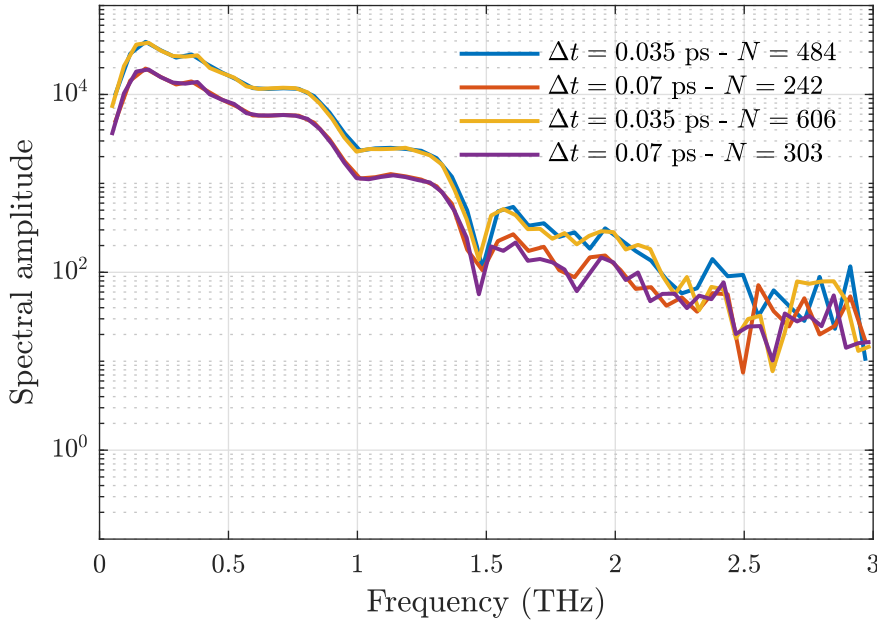


**Figure 2.16:** The spectral amplitudes of real data recorded with different  $\Delta t$  and  $N$  but pairwise same scan duration  $T$  to test the relation in Eq. (2.94).

### 2.3 Lock-in Amplification

The THz signal sampled by the detector is in the subnanoampere range and a lock-in is often used to restore the weak signal from the noisy environment and to improve the signal-to-noise ratio. Thus, the lock-in technique is crucial in THz-TDS and accordingly the following section inspired by [1; 14; 15; 16] is dedicated to give a brief overview of the functioning hereof.

Lock-in amplifiers are more or less complex analog or digital circuits, however, the concept can be divided into three fundamental stages being input amplification, signal filtering, and demodulation. The signal fed to the lock-in is amplified by a high-gain, low noise voltage amplifier. Some lock-in amplifiers may also provide a low noise current-to-voltage input. In this case, the current-to-voltage converter resembles a perfect ammeter, that is an active converter with zero input impedance. The filtering stage is where different lock-in amplifiers stands out. This stage can include a high-pass filter to reject low-frequency  $1/f$  noise, an auto-tracking bandpass filter locked to the internal reference frequency, and notch filters discarding first and second harmonic noise of the power grid. The third stage multiplies the now amplified and filtered signal by a reference signal in the demodulator. The reference signal is a clean sinusoidal signal at a fixed frequency matching the frequency of the signal to be measured. The product signal is passed to a low-pass filter averaging it continuously. Finally, the signal is fed to a DC amplifier to reach a  $\pm 10$  V output signal.

To exploit a lock-in amplifier the experiment has to be excited at a fixed reference frequency  $\omega_r$  causing the response to occur at the exact frequency  $\omega_r$  passed to the lock-in. A phase-locked loop (PLL) in the lock-in circuit generates an internal sinusoidal reference signal

$$V_{\text{ref}}(t) = V_L \sin(\omega_L t + \theta_r). \quad (2.96)$$

locked to the external signal. Given the measured signal is sinusoidal with amplitude  $V_s$  and phase  $\theta_s$  the input is

$$V(t) = V_s \sin(\omega_r t + \theta_s) \quad (2.97)$$

which is amplified and possibly filtered at the first stage of the lock-in amplifier. The response signal is not likely to be pure sinusoidal and noise will be present in a real experiment but as long as the signal is periodic with  $\omega_L$  the lock-in amplifier picks out the fundamental Fourier components.

At the second stage a phase-sensitive detector (PSD) multiplies the signal by the internal lock-in reference signal

$$\begin{aligned} V_{\text{PSD}}(t) &= V_s V_L \sin(\omega_r t + \theta_s) \sin(\omega_L t + \theta_r) \\ &= \frac{1}{2} V_s V_L \{ \cos((\omega_r - \omega_L)t + \theta_s - \theta_r) - \cos((\omega_r + \omega_L)t + \theta_s + \theta_r) \} \end{aligned} \quad (2.98)$$

resulting in two AC signals at frequencies  $\omega_r \pm \omega_L$  and phase  $\omega_s \pm \omega_r$ , respectively. The subsequent low-pass filter averages the signal over a span  $T$

$$\langle V_{\text{PSD}} \rangle = \frac{1}{T} \int_0^T V_{\text{PSD}}(t) dt = \frac{1}{2} V_s V_L \left( \frac{\sin((\omega_r - \omega_L)T + \theta_s - \theta_r)}{(\omega_r - \omega_L)T} - \frac{\sin((\omega_r + \omega_L)T + \theta_s + \theta_r)}{(\omega_r + \omega_L)T} \right). \quad (2.99)$$

If the integration interval is long compared to the period of the signal  $T$  approaches infinity and both terms will clearly approach zero. However,  $\omega_r - \omega_L \ll \omega_r + \omega_L$ , hence, the second term converges more rapidly than the first. The integration interval is set at the time constant section of the lock-in amplifier, and clearly, longer time constants narrow the detection band increasing the noise rejection and vice versa. The disadvantage of a longer time constant is the corresponding longer time each measurement requires. This can easily add up since as a rule of thumb one should wait three to five time constants before a reliable measurement can be made.

The response signal to be restored has frequency  $\omega_r = \omega_L$ . Thus, the signal leaving the PSD is AC with a DC offset

$$V_{\text{PSD}}(t) = \frac{1}{2} V_s V_L \{ \cos(\theta_s - \theta_r) - \cos(2\omega_r t + \theta_s + \theta_r) \} \quad (2.100)$$

and with a proper choice of time constant the averaged signal becomes a pure DC signal proportional to the amplitude  $V_s$  of the response signal

$$\langle V_{\text{PSD}} \rangle = \frac{1}{2} V_s V_L \cos(\theta_s - \theta_r) \propto V_s \cos(\theta_s - \theta_r). \quad (2.101)$$

This equation shows why the phase-lock loop is so important for the lock-in technique. If the phase between the signals changed with time then  $\cos(\theta_s - \theta_r)$  would be time-dependent implying that  $V_{\text{PSD}}$  would not be a DC signal. Another feature of the phase-lock is the rejection of random noise at the reference frequency  $\omega_r$ , since the phase of random noise varies with time and thus averages to zero.

If the present noise has frequency  $\omega_n$  far from the reference frequency  $\omega_r$  neither  $\omega_n - \omega_r$  nor  $\omega_n + \omega_r$  are close to DC and the low-pass filter attenuates the noise components of the signal. Contrary, if  $\omega_n$  is close to  $\omega_r$  then  $\omega_n - \omega_r$  is small implying the bandwidth of the low-pass filter has to be narrow the attenuate the very low-frequency AC noise signal. This doesn't affect the response signal due to its true DC nature.

Eq. (2.101) shows that the measurement  $V_s \cos \theta$  depends on the phase difference  $\theta = \theta_s - \theta_r$  between the signal and the internal reference signal. Hence, adjusting  $\theta_r$  such

### 2.3. Lock-in Amplification

that  $\theta$  equals zero then the measured signal is obviously  $V_s$ . This also means that if  $\theta = 90^\circ$  then the output is zero. In general lock-in amplifiers are calibrated to display the input and output signals in volts rms and not peak. It is possible to circumvent the phase-dependency if an additional PSD is inserted in the lock-in circuit and shifting the reference signal fed to this PSD  $90^\circ$

$$V_{\text{PSD2}}(t) = V_s V_L \sin(\omega_r t + \theta_s) \cos(\omega_L t + \theta_r) \quad (2.102)$$

$$\langle V_{\text{PSD2}} \rangle = \frac{1}{2} V_s V_L \sin(\theta_s - \theta_r) \propto V_s \sin \theta. \quad (2.103)$$

The two low-pass filtered outputs

$$X = V_s \cos \theta \quad \text{and} \quad Y = V_s \sin \theta \quad (2.104)$$

form a vector relative to the internal reference signal  $V_{\text{ref}}$  and are referred to as the in-phase and the quadrature component, respectively, due to the fact that  $X$  measures the signal while  $Y$  is zero when  $\theta = 0$ . The magnitude of the signal vector is

$$R = \sqrt{X^2 + Y^2} = V_s, \quad (2.105)$$

i.e. equal to the amplitude of the signal to be restored and not least phase independent, while the phase between the  $V$  and  $V_{\text{ref}}$  can be calculated as

$$\theta = \arctan \left( \frac{Y}{X} \right). \quad (2.106)$$

self-evident, lock-in amplifiers with a single PSD circuit are called single-phase lock-ins whereas lock-in amplifiers with a double PSD circuit and orthogonal reference oscillators are called dual-phase lock-ins. Not only is it possible to measure  $X$  and  $Y$  with dual-phase lock-in amplifiers but also  $R$  and  $\theta$  are measured directly which is a great advantage over single-phase lock-in amplifiers.

The dynamic reserve parameter is unquestionable important to understand when utilising lock-in amplifiers to restore weak signals in a noisy environment. It is defined in dB as the ratio of the largest acceptable noise signal  $V_n$  to the full-scale signal  $V$

$$\text{Dynamic Reserve (in dB)} = 20 \log_{10} \left( \frac{V_n}{V} \right). \quad (2.107)$$

The dynamic reserve is, hence, an expression of how much noise that can be present before an incorrect signal is measured by the lock-in amplifier. This definition can be a bit vague or ambiguous, since the definition of the largest acceptable noise signal  $V_n$  can vary. However, it is usually defined as levels which utmost influence the output signal of the lock-in amplifier by a few percentages of the full-scale signal  $V$ . Consequently, the dynamic reserve controls the gain distribution throughout the lock-in amplifier, thus, make it possible to prevent a potential overload in any part of the lock-in circuit. A high dynamic reserve corresponds to a very low amplification of the input signal such that more noise can be present before the input channel overloads and most of the overall amplification is redistributed to happen after the low-pass filter to the DC signal. This entails that the signal fed to the PSD is equally small and large noise components are attenuated by the low-pass filter. Analog lock-in amplifiers are limited to a maximum dynamic reserve of 60 dB by gain redistribution but an additional 20 dB can be achieved by a bandpass filter in the input section of the circuit. The upper limit is due to linearity and DC offset problems occurring in analog PSDs at very small input signals and in DC amplifiers driven

at very high gain. The dynamic reserve depends on the noise frequency  $\omega_n$  relative to the reference frequency  $\omega_r$ , since noise at the reference frequency will not be rejected by the low-pass filter whereas other noise components are rejected implying that the dynamic reserve is 0 dB at  $\omega_n = \omega_r$  increasing as  $\omega_n$  changes. The rate of change of the dynamic reserve is determined by the time constant and the roll-off of the low-pass filter. The levels quoted on the lock-in amplifier are given for noise frequencies, where the dynamic reserve limit is set by the distribution of the gain and the overload level of each part of the circuit, i.e. far from the reference frequency.

### 3. Terahertz Time-Domain Spectrometer

In this chapter the experimental work made during this semester to optimise and benchmark the spectrometer designed and constructed in my ninth semester project last semester, see [1], is presented. Initially, the original spectrometer design is introduced followed by the improvements hereof. Subsequent, the software written for the data acquisition and the data analysis are briefly accounted for, before the settings of the spectrometer, including the lock-in amplifier, are tested and a set of recommended default settings are given. Then, the results of the benchmark of the optimised spectrometer are presented, and finally, an overall evaluation of the spectrometer performance is given.

#### 3.1 Spectrometer Design

Figure 3.1 illustrates the experimental setup constructed in the previous semester.

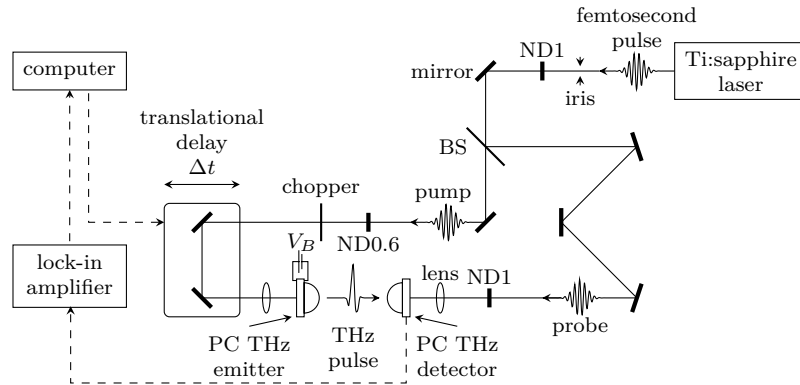


**Figure 3.1:** Scheme of the spectrometer design from the ninth semester project [1].

A Ti:sapphire Tsunami femtosecond laser from Spectra Physics supplies short laser pulses (800 nm center wavelength,  $\sim 85$  fs pulse width, 1 W of average power, and 80 MHz repetition rate) to the optical system. Before a 35/65 beam splitter (BS) divides the pulses into a pump and a probe branch, an iris and a reflective neutral density filter with optical density 1.0 (ND1) prevent the femtosecond pulses from running back into the laser and adjust the average power of the beam to match the ratings of the PCAs utilised as THz emitter and receiver. The photoconductive antennas are from BATOP Optoelectronics. The emitter and the detector have an dipole and a bow-tie geometry, respectively. A ND1 filter is placed before the THz detector for further adjustment of the average beam power. The laser pulses in the pump branch were initially sent through a ND0.6 filter to reduce power at the emitter, this, however, was removed, thus running the PCA at higher power, in order to find the THz signal in the possibly faulty system. Next, the pump pulses pass a rotating optical chopper exciting the THz emitter at a fixed reference frequency forwarded to a SR530 lock-in amplifier from Stanford Research Systems. Prior to the THz source a translational stage adjusts the relative time delay  $\Delta t$  controlled with an Arduino Uno micro controller board by a homemade computer software. In both branches, lenses ( $NA = 0.16$ ,  $f = 13.84$  mm) focus the optical pulses in the photoconductive gap of the antennas. Photocarriers excited in the THz emitter by the femtosecond pulses are accelerated by an external DC bias voltage  $V_B$  across the antenna to generate broadband

THz pulses. The detector is unbiased, and the optical excited carriers are accelerated by the incoming THz pulses, thus, generating a photocurrent to be measured by the lock-in amplifier and afterwards collected by the same software controlling the delay line.

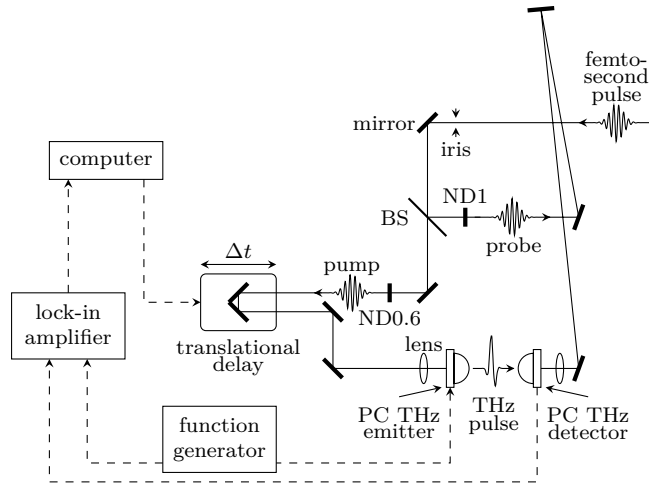


**Figure 3.2:** Scheme of the optimised spectrometer design.

During this thesis the design of the experimental scheme has been improved and reconstructed to optimise the performance of the spectrometer. The new scheme is shown in Figure 3.2. First, the Ti:sapphire laser power was increased from 1 W to 1.2 W at 800 nm. The beam was divided by a 82.5/17.5 beam splitter prior to the system due to the availability of other experiments. After the beam splitter, the femtosecond beam entering the spectrometer has an average power of 210 mW. The ND1 filter prior to the beam splitter of the spectrometer has been removed and the ND1 filter in the probe branch has been moved closer to the beam splitter, see Figure 3.2. The measured mean optical power hitting the photoconductive emitter and detector was approximately 13.7 and 10.8 mW, respectively. In [1] the focused beam diameter at the antennas was calculated to be  $2w_0 \approx 7\mu\text{m}$ , hence, the pulse fluence at the photoconductive gap of the emitter is  $445 \mu\text{J}/\text{cm}^2$  and of the detector  $350 \mu\text{J}/\text{cm}^2$  calculated by

$$F = \frac{P_{\text{avg}}/f_{\text{rep}}}{\pi w_0^2} \quad (3.1)$$

where  $P_{\text{avg}}$  is the optical mean power,  $f_{\text{rep}} = 80 \text{ MHz}$  is the laser repetition rate, and  $D$  is the beam diameter [1]. The pulse fluence is within the recommended range of the detector ( $250\text{-}500 \mu\text{J}/\text{cm}^2$ ), but above the maximum rating given for the emitter ( $200\text{-}250 \mu\text{J}/\text{cm}^2$ ) [17; 18]. This has, however, been necessary to generate any pulse from the emitter.

Closer investigations of the emitter revealed vital problems with the soldering of the shield of the coaxial cable to the antenna electrodes contact pad. The soldering was poorly made and only a few wires of the coaxial shielding had been attached, which eventually have ruptured. Thus, the connection relied on transients and proper position of the cable, such that the shielding is pressed against the contact pad. Clearly, this will not do and the soldering had to be repaired.

Secondly, the probe branch has been extended, such that the detector is located closer to the last probe mirror allowing either focusing TPX lenses or parabolic mirrors and a sample to be installed between the THz source and the THz receiver, if needed.

### 3.2. Data Acquisition and Analysis

The stability of the setup has been improved by replacing the two mirror constituting the delay line together with a translational stage with a 25.4 mm clear aperture, 5 arcsec, gold retroreflector from Edmund Optics.

Another major development of the experimental setup is the substitution of the rotating optical chopper by a TG550 function generator from TTi implying the THz signal is chopped electrical by switching the bias voltage across the emitter on and off at a given fixed reference frequency instead of chopping the optical pulses resulting in a significantly broader reference frequency range. This allows a reference frequency in the range of 10 kHz versus the 350 Hz of the optical chopper, which is preferable for various reasons. Not only does 10 kHz seem to be the most common reference frequency among others in the field, but the response is also much faster.

Finally, care have been taken to align the optical system, such that the optical beam is incident and focused orthogonally on the photoconductive gap to ensure a correct generation of the THz pulse relative to the substrate lens, and in that connection it has been possible to achieve a better alignment at the detector resulting in a higher signal-to-noise ratio. The relative alignment of the THz source to the THz receiver has also been adjusted for maximum THz power at the detector.

### 3.2 Data Acquisition and Analysis

The output of the lock-in amplifier is connected the computer through an ADLINK PCI-9111DG D/A converter. Originally, Research Technician Peter Kjær Kristensen from the Department of Physics and Nanotechnology at Aalborg University wrote the C Sharp and the Arduino software, which control the stage and collect the data from the lock-in amplifier. However, during the ninth and the present semester the C Sharp software has been modified to include features such as setting the number of time constants that should pass, before a measurement is made, and the number of scans that are averaged. Another improvement is the export function, which didn't comply with the small values of the measurements. A screenshot of the user interface is seen in Figure 3.3.

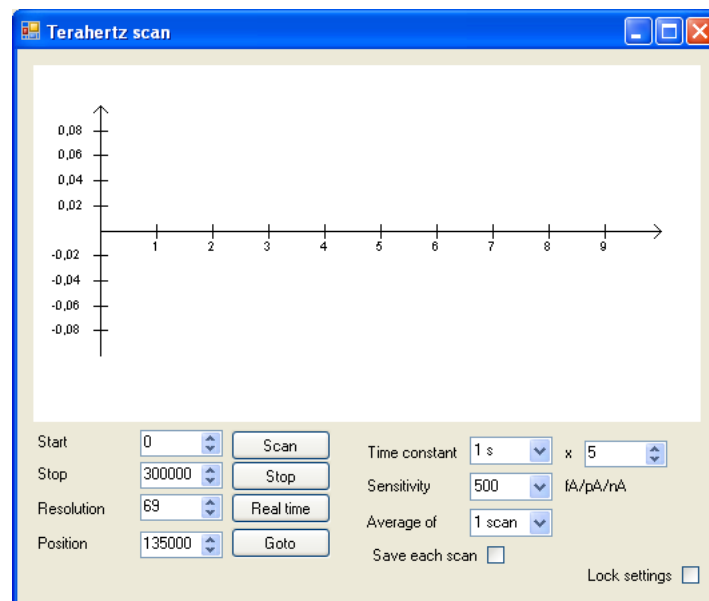


Figure 3.3: Screenshot data collection

The *Start*, *Stop*, *Resolution*, and *Position* boxes are set in terms of the steps of the stage motor. The outer positions of the motor is at zero and 310,000 steps. The stage is located such that the zero time delay position ( $\Delta t = 0$ ) is at 135,000 steps. If the motor is set between zero and 135,000 steps the pump pulses arrive at the emitter after the probe pulses have arrived at the detector, and reverse between 135,000 and 310,000 steps. The *Position* box is used in combination with either the *Goto* or the *Real time* buttons. With the latter measurements are read out at the given position in even intervals according to the time constant.

Two boxes control the *Time constant* settings. The first box should be set at the lock-in amplifier predetection time constant. The second box is the software time constant  $TC_s$ , that is, the time waited before each measurement is read out from the lock-in amplifier.

The lock-in amplifier output is amplified to a  $\pm 10$  V scale, and hence, the data acquired by the software have to be converted back to the original scale set at the lock-in amplifier. This is done by the *Sensitivity* box which should match the chosen sensitivity setting of the lock-in amplifier.

Lastly, the *Average of* box sets the number of consecutive scans that are averaged. Each scan can optionally be saved separately.

Eventually, a large amount of data is recorded, and a MATLAB program with an associated user interface have been written to make the data handling and analysis much easier and more consistent. A screenshot of the MATLAB program is found in Figure 3.4. The

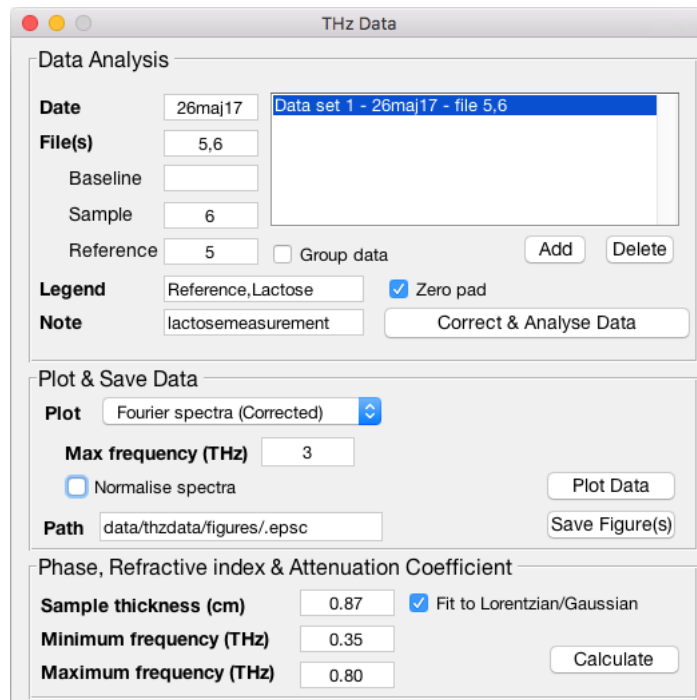


**Figure 3.4:** Screenshot of the GUI of the MATLAB code writing to analyse and plot the data consistently.

data files from the data acquisition software consist of two columns; one containing the stage position given in steps ranging from zero to 310,000 and one containing the measured photocurrent in picoamperes.

When data is imported to the program, the stage position and the photocurrent of the

### 3.2. Data Acquisition and Analysis

traces of each data set are stored in two cell arrays  $\mathbf{x}$  and  $\mathbf{y}$ , respectively, each containing the vectorised data. If two traces of  $N$  points are imported as in Figure 3.4,  $\mathbf{x}$  and  $\mathbf{y}$  will be  $1 \times 2$  cell arrays, and each cell of  $\mathbf{x}$  and  $\mathbf{y}$  contains a vector of length  $N$ .

Initially, the stage position data  $\mathbf{x}$  of each trace  $j$  are translated into a relative time delay in picoseconds by

```
for j = 1:length(x)
    t{j} = (x{j}-135e3)/310e3*2*4.9e-2/3e8*1e12;
end
```

where  $4.9e-2$  is the total stage length in meters and  $3e8$  is the speed of light in vacuum. The factor of two is due to the double length the pulses have to travel in the delay line.

The current data is corrected for any offset by the simple code

```
offset = cellfun(@sum,y)./cellfun(@length,y);
for j = 1:length(y)
    ycorrected{j} = y{j}-offset(j);
end
```

The data points  $\mathbf{y}$  of each trace  $j$  are summed and divided by the number of points in each trace  $\text{length}(\mathbf{y}\{j\})$ . The result `offset` is the mean offset per data point, which subsequent is subtracted from each data point. The second step is the Fast Fourier Transform.

```
for j = 1:length(y)
    L = length(y{j});
    Nfft = 2^nextpow2(L);
    if ~zeropad, Nfft = L;
    end
    Deltat = abs(t{j}(2)-t{j}(1));
    fs = 1/Deltat;
    Deltaf = fs/Nfft;
    f = Deltaf*(1:floor(Nfft/2))';
    dft = fft(y{j},Nfft);
    phi = angle(dft);
    phi = unwrap(phi');
    phi = phi(2:length(f)+1);
    dft = abs(dft);
    dft = dft(2:length(f)+1);
    dft(1:end-1) = 2*dft(1:end-1);
end
```

If zero padding is checked in the GUI, the program calculates the next power of two `Nfft` of the number of data points  $L$ , which is used in the FFT afterwards. Otherwise, `Nfft` is set equal to the actual number of data points  $L$ . The scan resolution  $\Delta t$  between each measurement is extracted from the data by `abs(t{j}(2)-t{j}(1))` to calculate the sampling rate  $\nu_s = 1/\Delta t$  (in the code, `fs`), which is utilised to calculate spectral resolution  $\Delta \nu$  (`Deltaf`) and eventually the vector of discrete frequencies  $\mathbf{f}$ . Note, that the one-sided spectrum is calculated with the DC frequency  $\nu = 0$  omitted, i.e. only positive frequencies up to and including the Nyquist frequency are employed. The `Nfft` point discrete Fourier transform of the  $j$ th data trace is computed by the build-in FFT algorithm `fft()`, from which the phase `phi` is extracted and unwrapped by `angle()` and `unwrap()` before adjusted

to the one-sided Fourier spectrum. Finally, the spectral amplitude is calculated by the absolute value `abs()` of the complex-valued data and adjusted to the frequencies. Since only the one-sided spectrum is calculated, all of the frequency components except the Nyquist frequency are multiplied by two.

The discrete Fourier transformation `dft` of each trace is stored in a cell array `Y`, which is then optionally normalised according to

```
M = cellfun(@max,Y);
m = cellfun(@min,Y);
for jj = 1:length(Y);
    YN = cellfun(@(s)(s-m(jj))/(M(jj)-m(jj)),Y,'UniformOutput',0);
end
```

where `YN` is a cell array of the normalised Fourier transformations. This is done for easier comparison of the individual frequency spectra.

### 3.3 Lock-in Amplifier and Scan Settings

As explained, a lock-in amplifier is required to measure the weak photocurrent at the detector, however, the settings of the lock-in amplifier have a substantial impact on the signal-to-noise ratio of the recorded signal. It should also be clear from the simulations in Section 2.2.3 that the scan resolution  $\Delta t$  affects the outcome. To test the effect of each parameter, default settings have been chosen as in Table 3.1.

Default Settings	
Scan duration	63 ps
Scan resolution	0.17 ps
No. of scans	1
Software time constant	3
Sensitivity	500 pA
Dynamic reserve	Normal (40 dB)
Input filters	OOO, see below
Predetection time constant	300 ms
Postdetection time constant	none
Reference frequency	10 kHz

**Table 3.1:** *Default settings of the lock-in amplifier and the recorded traces.*

The time-domain pulse and the corresponding spectral amplitude recorded with the default settings are shown in Figure 3.5 and 3.6. Notice the rather long pulse of  $\sim 10$  ps. The bump in the time-domain signal around  $-20$  ps, which one normally would contribute to reflections, and the odd bump just below  $-40$  ps may be due to electrical reflections at the contact pads of the emitter, since no sample is present to cause such reflections, and the impedance corrections of the antenna may be affected due to the required resoldering as mentioned above. However, these features of the pulse shape should not be a problem, since they occur consistently.

The normalised frequency spectrum shows that the bandwidth of the detector is roughly 0.8 THz starting from 0.2 up to 1.4 THz before hitting the noise floor, which is in good

### 3.3. Lock-in Amplifier and Scan Settings

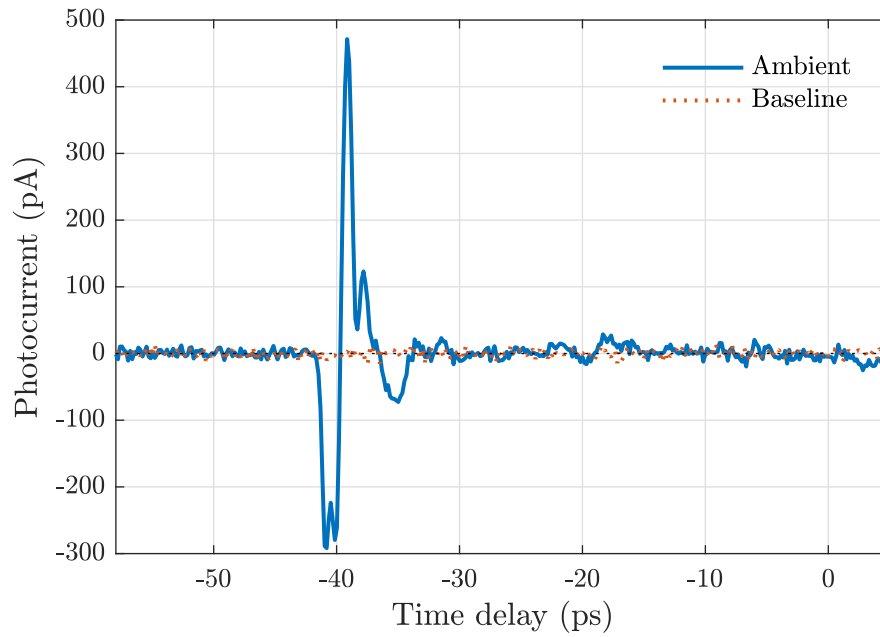


**Figure 3.5:** The THz pulse recorded in the time-domain with the default settings listed in Table 3.1.

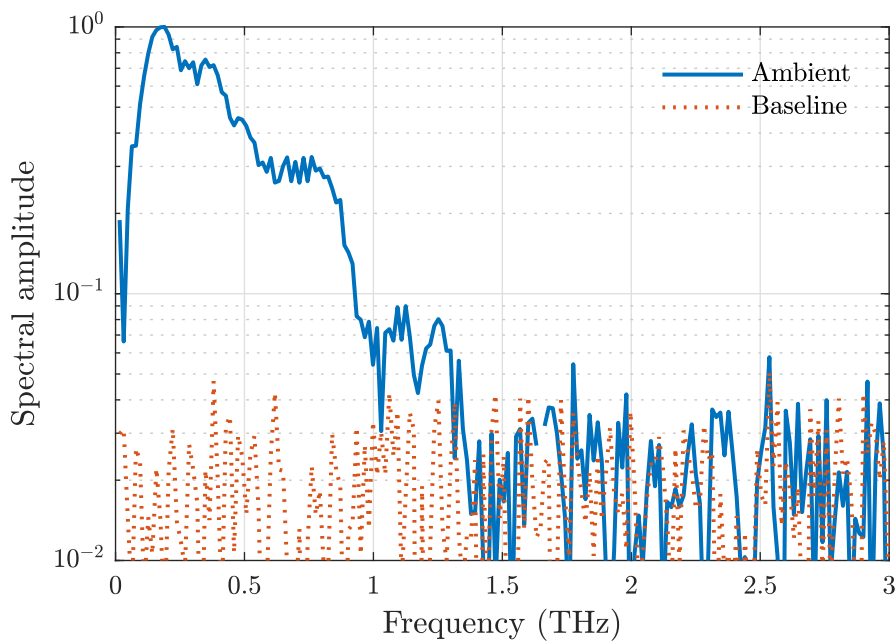


**Figure 3.6:** The frequency spectrum of the THz pulse recorded in the time-domain with the default settings listed in Table 3.1 (top) and the corresponding frequency spectrum (bottom).

agreement with the 10 ps pulse duration. That is; the THz pulse is rather narrow in bandwidth causing a wider pulse.

Three scans have been made with different frequencies of the square wave modulation of the bias field at 1 kHz (blue line), 10 kHz (red line), and 40 kHz (yellow line). The resulting normalised frequency spectrum is shown in Figure 3.7. At 1 kHz more noise is

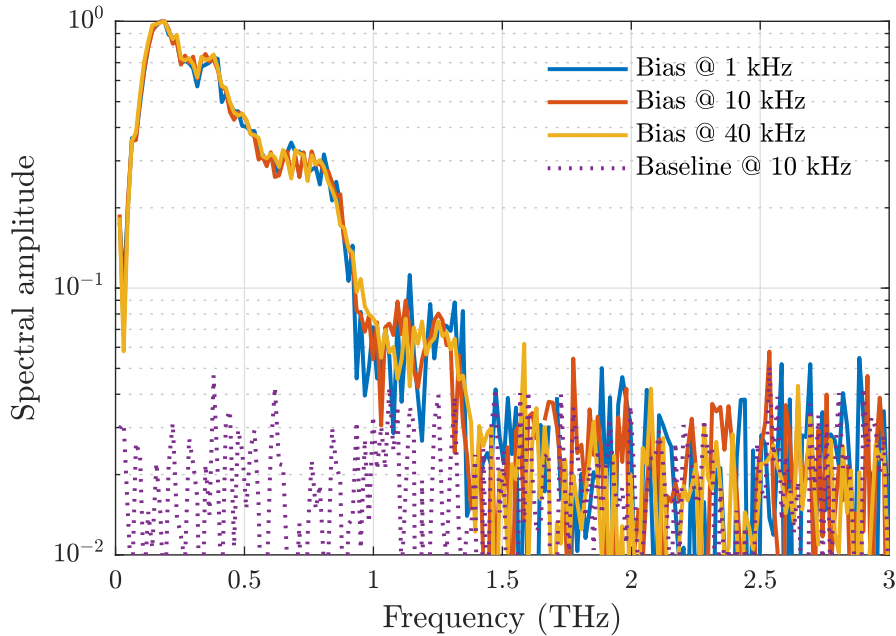


**Figure 3.7:** Spectral amplitude of three traces recorded with varying reference frequency of 1 kHz (blue line), 10 kHz (red line), and 40 kHz (yellow line).

present compared to the other scans, and the signal is affected just below 1 THz implying a narrower bandwidth, whereas the noise obscure the 10 and the 40 kHz signals at 1.3-1.4 THz. The 40 kHz generally seem to be slightly less affected by the noise, but the difference is not very distinct, and the 10 kHz is applied further on as recommended by BATOP.

In the previous chapter, it became clear, that the scan resolution  $\Delta t$  not only is important in order to resolve the time-domain pulse but also has a critical effect in terms of aliasing. Figure 3.8 shows three scans of different scan resolution; 0.08 ps (blue line), 0.17 ps (red line), and 0.33 ps (yellow line).

In all three cases, the scan resolution should be sufficient to resolve the THz pulse being roughly 10 ps wide. None of the scans show any strong signs of the alias effect. The Nyquist frequency of the blue line is 6.25 THz, and thus, the alias effect is not expected to be present at 3 THz. The Nyquist frequencies of the red and the yellow lines are approximately 3 and 1.5 THz, respectively, and if any aliasing effects were present, they should be evident from Figure 3.8. The yellow curve might suggest a slight aliasing just below 1.5 THz, however, this may as well just be noise. Yet, the frequency spectra do support the assumption that the THz pulse is rather narrowband than broadband, as it ought to be, since no strong aliasing is seen, i.e. the pulse does not possess any frequency components above 1.5 THz.

The lock-in amplifier has three different input filters that can be turned in and out of the circuit; an auto-tracking band-pass filter (IOO), a notch filter set at the line frequency (OIO), and a notch filter set at the second harmonic of the line frequency (OOI). In Figure

### 3.3. Lock-in Amplifier and Scan Settings

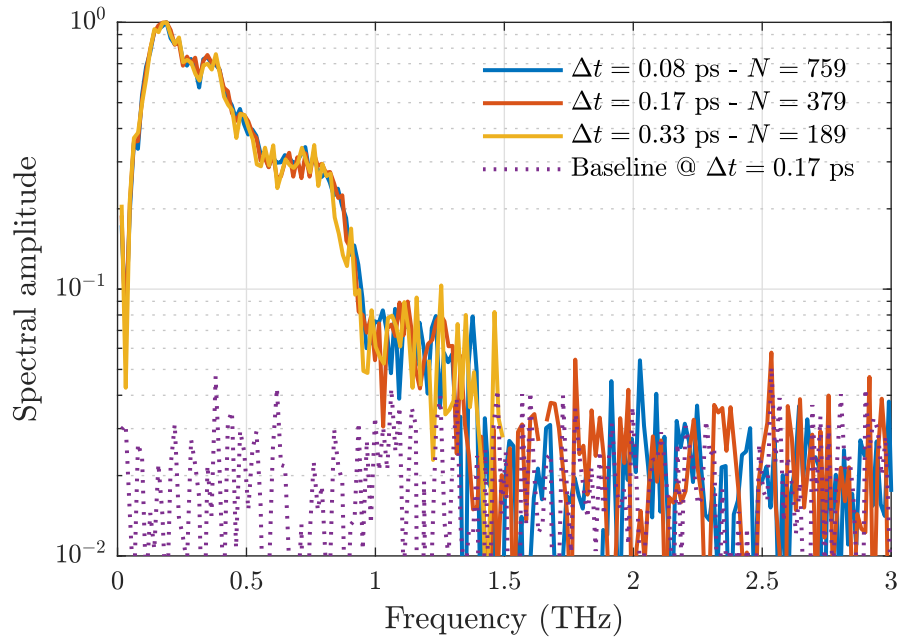


**Figure 3.8:** The spectral amplitude of three scans with different scan resolutions  $\Delta t$  of 0.08 ps (blue line), 0.17 ps (red line), and 0.33 ps (yellow line)

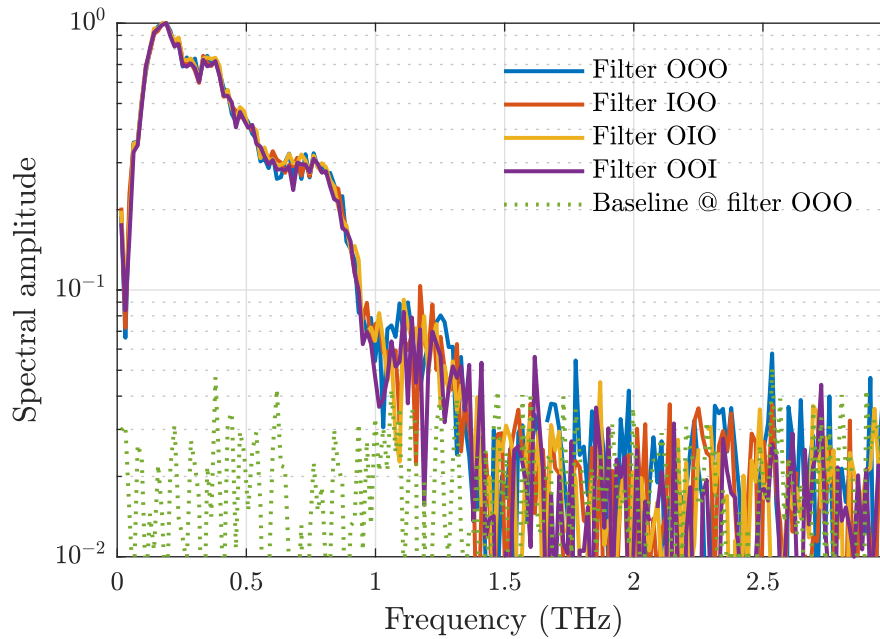


**Figure 3.9:** The spectral amplitude of four identical scans testing the effect of the lock-in amplifier input filters.

3.9, the first trace is recorded with no filters turned in (OOO, blue line) followed by traces with each filter individually turned into the circuit. None of the input filters have any distinct effect on the measured signal, and hence, they will not be coupled into the lock-in circuit in future measurements.

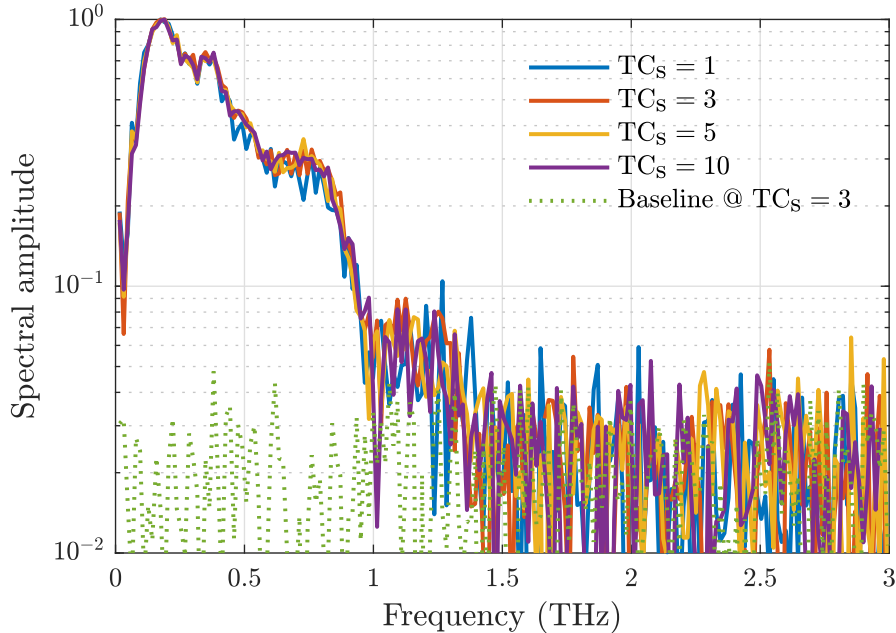


**Figure 3.10:** *The spectral amplitude of four identical scans but with different software time constants.*

The duration before each readout is important and is set by the software time constant  $TC_s$ . As a rule of thumb, the lock-in amplifier settles on a reliable measurement after three to five predetection time constants. The effect of the software time constant is investigated in Figure 3.10. Four scans are made. The software time constant is set to one (blue line), three (red line), five (yellow line), and ten (purple line) times the predetection time constant of the lock-in amplifier. Reading out the value after just one time constant entails a substantial amount of noise to the signal compared to the signal achieved after waiting three time constants. The effect of increasing the software time constant above three is present but not as notable as going from one to three time constants. In any case, the upper limit of the bandwidth is at 1 THz. Thus, one should consider the total scan duration versus the improvement before choosing a software time constant larger than three time constants per readout.

The predetection time constant sets the bandwidth of the lock-in low-pass filter following the PSD. Hence, this parameter has large impact on the signal, which is clear in Figure 3.11. The noise is drastically attenuated going from a predetection time constant of 100 ms (blue line) to just 300 ms (red line) and further to 1 s (yellow). However, above 1 s the effect decreases and yet again one should weigh the effect versus the total scan duration. The pulse bandwidth is slightly improved to cut off at 1.5 THz for predetection time constants above 300 ms.

Another low-pass filter can be turned into the lock-in circuit referred to as the postdetection low-pass filter, and its impact on the signal is investigated in Figure 3.12. The postdetection time constant can take three different values; none (blue line), meaning that the low-pass filter is switched off, 0.1 s (red line), and 1 s (yellow line). The effect of the

### 3.3. Lock-in Amplifier and Scan Settings

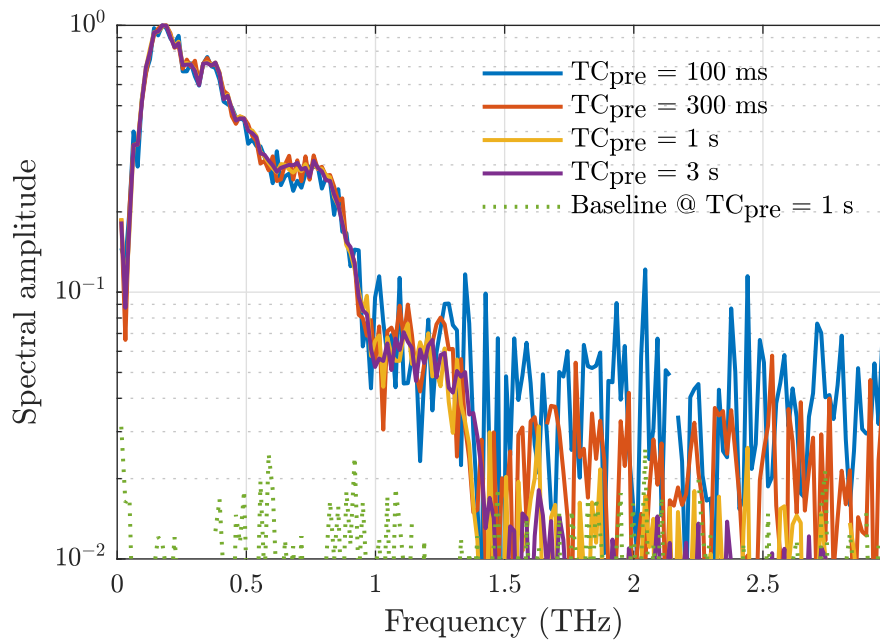


**Figure 3.11:** The frequency spectrum of four traces with different predetection time constants.

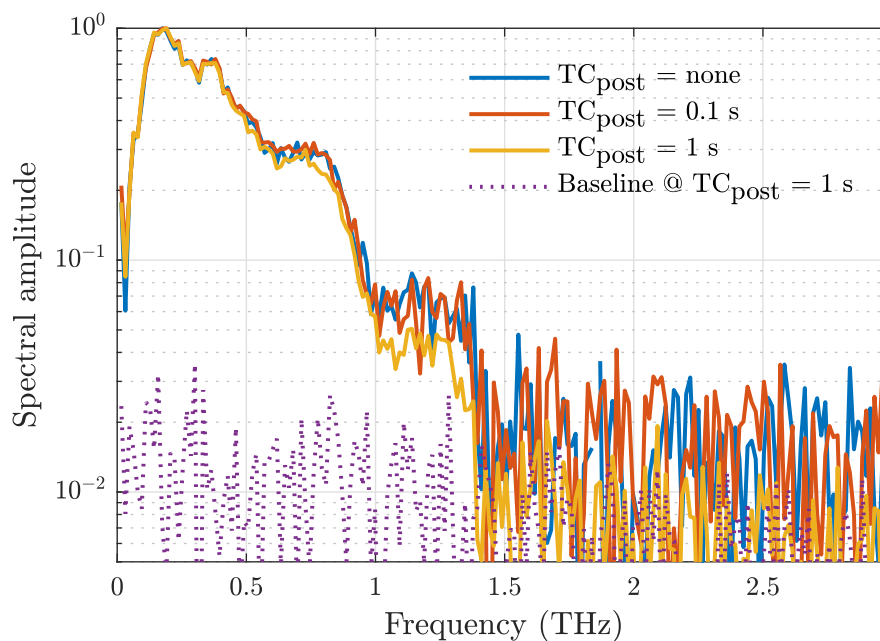


**Figure 3.12:** The effect of the lock-in amplifier postdetection low-pass filter is investigated by recording three identical traces with different post detection time constants.

1 s postdetection time constant is evident above 1 THz. The noise floor is substantially lowered and weak frequency components between 1 and 1.5 THz is possible to measure. To utilise a 1 s postdetection time constant one should ensure, that the software time constant times the predetection time constant is at least 1 s. When it is possible, the postdetection time constant should always be set to 1 s for a better signal-to-noise ratio.

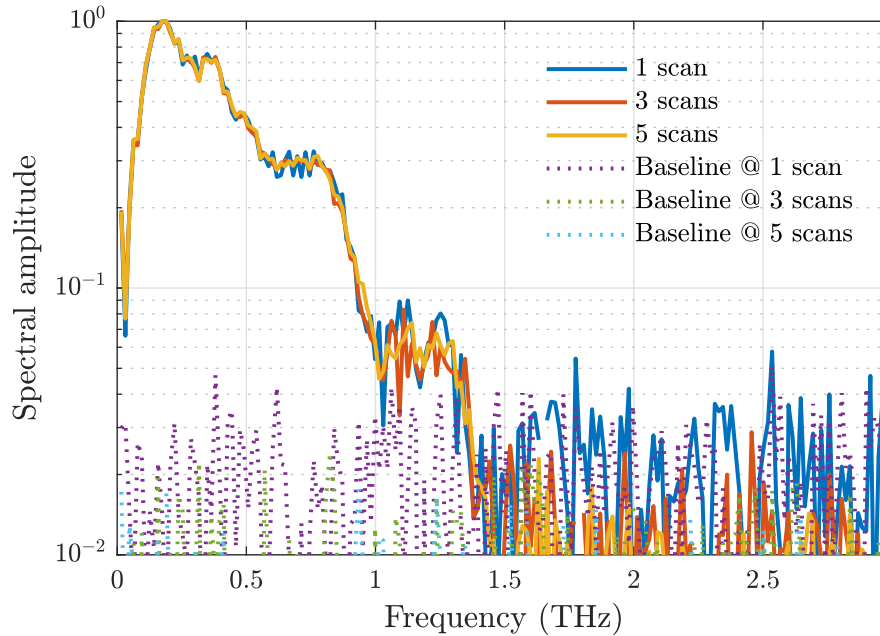


**Figure 3.13:** Three traces averaged over one, three, and 5 identical scans, respectively.

Fluctuations in the laser beam contribute to the overall noise, however, the noise due to these fluctuations can be lowered by averaging consecutive scans. The impact on the noise by averaging consecutive scans is investigated in Figure 3.13. Clearly, the noise floor is attenuated significantly when three consecutive scans are averaged. This helps to improve the upper limit of the bandwidth from 1 THz to roughly 1.5 THz. The noise is reduced even further if five consecutive scans are averaged, but the bandwidth of the THz pulse does not seem to extend above 1.5 THz. However, the effect of averaging more than three scans is small, which is to be expected, since random noise is reduced as  $1/\sqrt{N}$ , where  $N$  is the number of measurements.

Another test to be carried out in future work is the effect of the predetection time constant when three consecutive traces are averaged to reveal if it is possible to reduce the scan duration.

The results of the above studies of the optimal spectrometer settings are summed in Table

### 3.4. Benchmarking by Terahertz Absorption Spectra

Optimised Settings	
Scan duration	60 ps or more depending on the required spectral resolution.
Scan resolution	0.17 ps or less depending on the frequency of interest.
No. of scans	3
Software time constant	3
Sensitivity	500 pA depending on the pulse.
Dynamic reserve	Normal (40 dB)
Input filters	OOO
Predetection time constant	1 s
Postdetection time constant	1 s
Reference frequency	10 kHz

**Table 3.2:** *Optimal settings of the spectrometer.*

### 3.4 Benchmarking by Terahertz Absorption Spectra

With the construction and the settings of the spectrometer optimised, the next step is to benchmark the performance through THz absorption spectra.

E. R. Brown et al. report in [19] measurements of a strong and narrow absorption signature in the microcrystalline form of  $\alpha$ -lactose monohydrate powder centered around 0.53 THz with a signature width just above 20 GHz. According to [19] such narrow signatures are generally weak, and thus, harder to distinguish from other absorption signatures. Since the signature is strong and lies within the bandwidth possible to achieve with the spectrometer in this work, and furthermore, lactose powder is very common and accessible, this is a very clear-cut choice of benchmark.

The samples in [19] were prepared by mixing pure  $\alpha$ -lactose monohydrate powder L2643 from Sigma Aldrich in a fine polyethylene (PE) powder MPP-620XXF from Micro Powders Inc. or Teflon powder with a mass proportion of 1:9 corresponding to 10% dilution or 1:4 corresponding to 20% dilution and then pressed into a pellet. Control samples of pure PE or Teflon powder were prepared likewise. The spectrometric techniques utilised in the article produce transmission spectra  $T(\nu)$  through the lactose samples which are normalised to the spectrum  $T_0(\nu)$  of the respective control sample correcting reflective and scattering effects in the transmission, which do not depend exponentially on the sample thickness  $d$ . Hence, the remaining attenuation is associated with absorption due to the lactose. Finally, the attenuation coefficient

$$\frac{1}{d} \log \left( \frac{T(\nu)}{T_0(\nu)} \right) \quad (3.2)$$

is plotted. The results obtained in [19] for a 1.59-cm-thick sample of  $\alpha$ -lactose monohydrate diluted to 10% in polyethylene powder by a tuneable frequency-multiplier-chain spectrometer with resolution of  $\sim 0.5$  MHz are presented in Figure 3.14. The data have been fitted with the Gaussian function

$$\varphi_G(\nu) = a \exp \left[ -b(\nu - \nu_0)^2 \right] \quad (3.3)$$

usually associated with inhomogeneous damping and the Lorentzian function

$$\varphi_L(\nu) = \frac{a}{1 + b(\nu - \nu_0)^2} \quad (3.4)$$

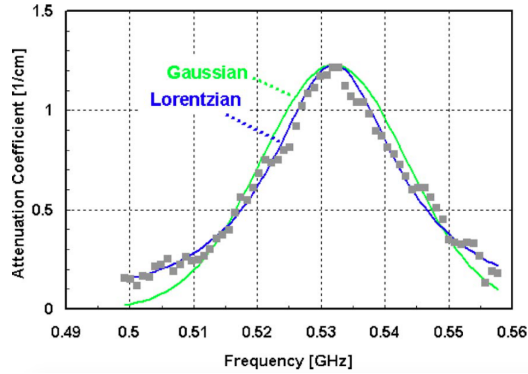


**Figure 3.14:** Figure from [19] showing experimental data and curve fits for the attenuation constant of a 10%  $\alpha$ -lactose monohydrate diluted in PE and pressed into a 1.59-cm-thick pellet. The center frequency  $\nu_0$  is  $532(\pm 1)$  GHz and the linewidth of the Lorentzian curvefit is  $24(\pm 1)$  GHz and  $27(\pm 1)$  GHz of the Gaussian fit. Clearly, the Lorentzian function is the best fit.

associated with homogeneous damping where  $a$ ,  $b$ , and the center frequency  $\nu_0$  are fitting parameters.

The same two kinds of fitting will be made in this work to determine the center frequency and the full width at half maximum (FWHM). However, MATLAB seems to struggle with the Lorentzian fit of the form given in Eq. (3.4). Rewriting the Lorentzian function as

$$\varphi_L(\nu) = \frac{a}{b + (\nu - \nu_0)^2} \quad (3.5)$$

solves the problem and has no effect on the resulting fit apart from the way the FWHM is calculated. In the form of Eq. (3.5) the FWHM is computed as [20]

$$\text{FWHM}_L = 2\sqrt{b}. \quad (3.6)$$

The Gaussian fit follows Eq. (3.3), and the FWHM is calculated as [21]

$$\text{FWHM}_G = 2\sqrt{\frac{\ln 2}{b}}. \quad (3.7)$$

Brown et al. conclude that the resonant attenuation signature of  $\alpha$ -lactose monohydrate around 530 GHz has FWHM just above 20 GHz and a better fit by the Lorentzian corresponding to a homogeneous damping associated with a collective vibrational transition that avoids fast scattering mechanisms, which normally occur, possible because of a significant reduction in phonon-phonon scattering.

### Characterisation of Lactose at 0.53 THz

In order to reproduce the results by Brown et al., and thereby verify that the noncommercial spectrometer, designed and constructed in [1] and optimised in this project, performs accurately and the data analysis is done right, the exact same  $\alpha$ -lactose monohydrate powder from Sigma Aldrich and the polyethylene powder from Micro Powders Inc. have been bought.

The lactose powder is diluted to 10% in PE powder by weighing 2.0 grams of lactose and 18.0 grams of PE followed by a meticulous mixing with a stainless steel spatula. A manual

### 3.4. Benchmarking by Terahertz Absorption Spectra

mounting press of 25 mm in diameter from Struers ApS is utilised to fabricate the pellets. Each pellet is made of 5.0 grams of either pure PE powder for the reference sample or 10% lactose powder for the lactose sample. The resulting base and cap surfaces of the cylindrical pellets are not completely flat (parallel) and smooth. Therefore, each sample is subsequently grinded and polished to a well-defined thickness  $d$  of 8.7 mm with smooth and parallel plane surfaces. Afterwards, the samples are properly cleaned with ethanol.

Each sample is attached between two retaining rings in a 25.4 mm aluminum lens tube, which is subsequently mounted on the THz detector, positioning the sample roughly midway between the THz emitter and the THz detector. No additional lenses are applied to the commercial emitter and detector whereby the THz beam is collimated with a beam diameter  $\sim 22$  mm. Two traces are recorded shown in Figure 3.15; one with the pure

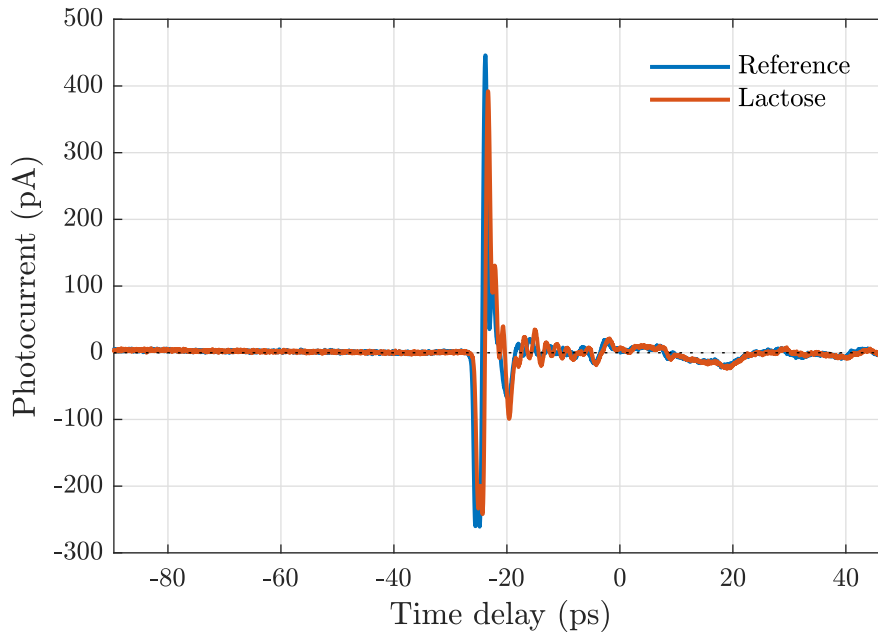


**Figure 3.15:** THz-TDS measurement reference and sample signals. The reference is a pure polyethylene pellet, and the sample is  $\alpha$ -lactose monohydrate diluted to 10% in polyethylene powder.

PE reference sample and one with the 10% lactose sample. Each trace has a scan duration  $T = 137$  ps with a scan resolution  $\Delta t = 35$  fs giving approximately 3900 data points per trace, and each trace is an average of three successive scans. Thus, the total data acquisition requires more than 23,400 lock-in measurements. This gives a spectral resolution

$$\Delta\nu = \frac{1}{T} \approx 7 \text{ GHz} \quad (3.8)$$

and a Nyquist critical frequency

$$\nu_c = \frac{1}{2\Delta t} \approx 14 \text{ THz} \quad (3.9)$$

preventing aliasing. None of the input filters of the lock-in amplifier are turned into the circuit, and the dynamic reserve is set to 40 dB. Both the pre- and the postdetection time constants of the lock-in amplifier are set to 1 s for a signal-to-noise ratio of nearly 20 dB at 530 GHz. The software time constant  $TC_s$  is set to three times the predetection time constant, i.e. 3 s, thus, the overall data acquisition time is roughly 20 hours with samples swapped midway.

When the recorded time-domain signals are examined it is clear that the lactose sample (red line) influences the THz pulse shape compared to the reference sample (blue line); the peak amplitude of the lactose trace at approximately  $-25$  ps is attenuated by approximately 50 pA, and oscillations are introduced mainly from  $-20$  ps to  $-5$  ps.

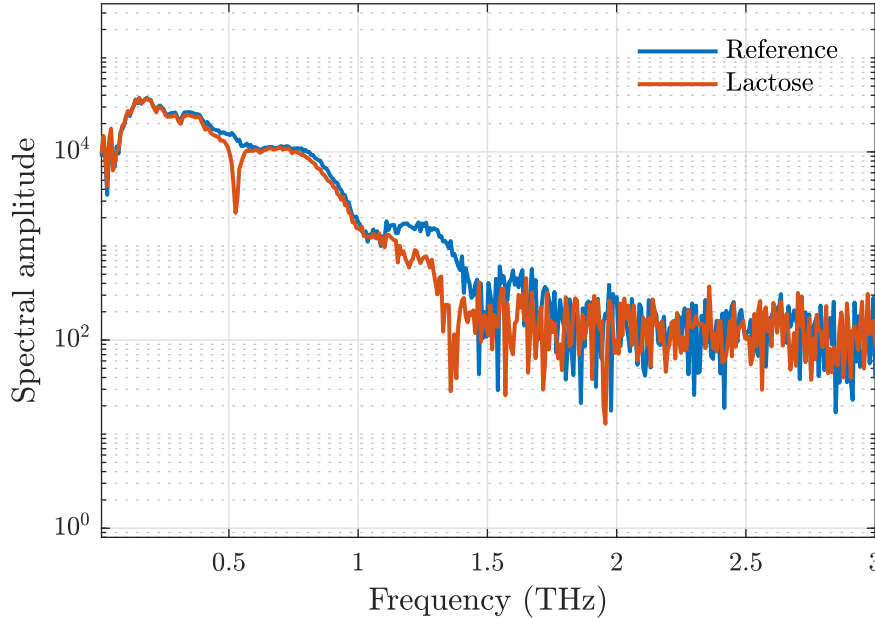


**Figure 3.16:** *The spectral amplitude of the reference (pure polyethylene) and sample (10%  $\alpha$ -lactose monohydrate in polyethylene) signals*

In Figure 3.16 the experimental data are Fourier transformed into the frequency-domain. The spectral amplitude of the lactose sample reveals a narrow but strong absorption signature near 0.5 THz. Furthermore, there is a weak indication of an attenuation signature between 1.3 and 1.4 THz, but the signal-to-noise ratio is below 10 dB in this frequency range, wherefore it is hard to conclude. However, a very strong signature is reported in the exact same range by Brown et al. in [19].

The attenuation coefficient is computed according to Eq. (3.2) and plotted together with the transmission phase in Figure 3.17. The attenuation coefficient is evidently obscured by noise from approximately 1.4 THz. In accordance with the observations in the spectral amplitude a narrow attenuation signature is present just above 0.5 THz. However, it is hard to distinguish a clear resonance in the transmission phase at the frequency. The transmission phase seem to exhibit an oscillating nature around 0.5 THz and above 1 THz which may be due to reflections in the reference and sample signals [13].

A zoom in is made on the signature around 0.53 THz in Figure 3.18, and data are fitted with the Lorentzian function (black line) and the Gaussian function (green line). Yet, it is still not possible to recognise any resonance in the transmission phase. Evidently, the Lorentzian function describes the attenuation signature better than the Gaussian function as expected. Both line fits predict a center frequency at  $526(\pm 7)$  GHz in good agreement with [19]. The FWHM of the Gaussian fit is  $32(\pm 7)$  GHz whereas the Lorentzian fit predicts a FWHM of  $26(\pm 7)$  GHz. These predictions are also in very good agreement with Brown et al.

The granularity of the frequency is improved in the search of a resonance in the transmission phase by zero padding the THz-TDS measurements to the next order of two before the

### 3.4. Benchmarking by Terahertz Absorption Spectra

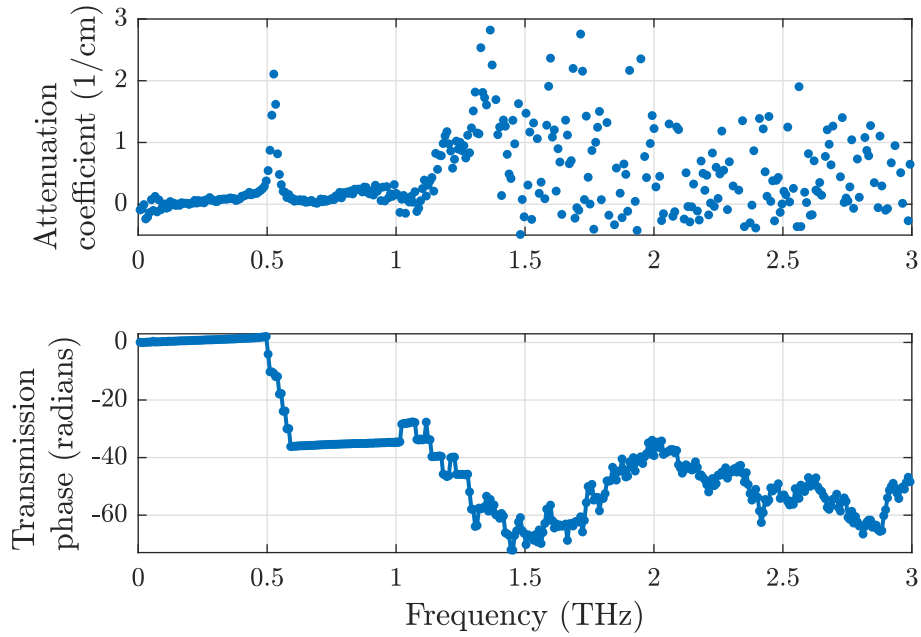


**Figure 3.17:** The computed attenuation coefficient and the transmission phase of the sample (10%  $\alpha$ -lactose monohydrate in polyethylene).

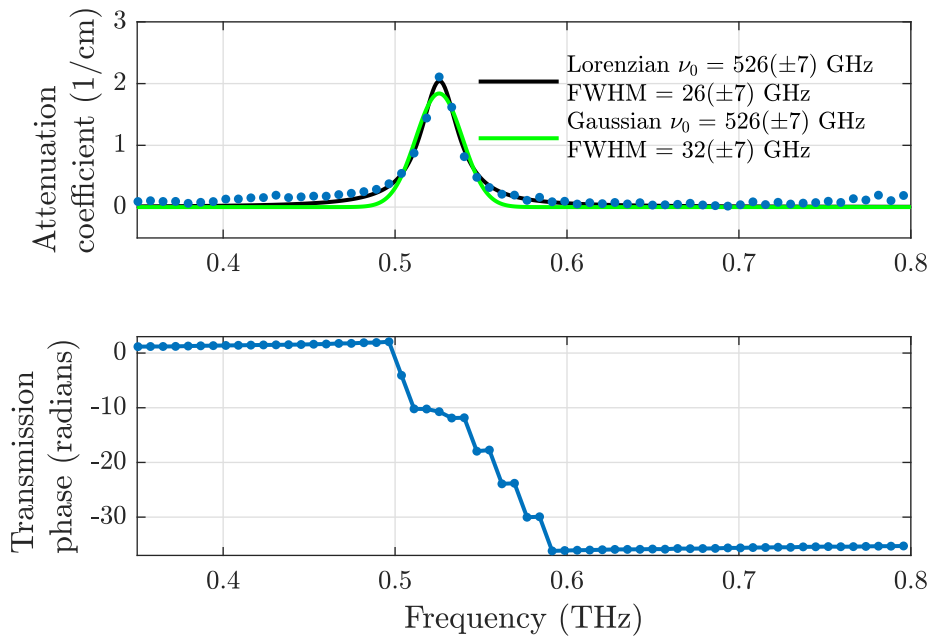


**Figure 3.18:** Zoom in on the 0.53 THz signature of the attenuation coefficient and the transmission phase of the sample (10%  $\alpha$ -lactose monohydrate in polyethylene).

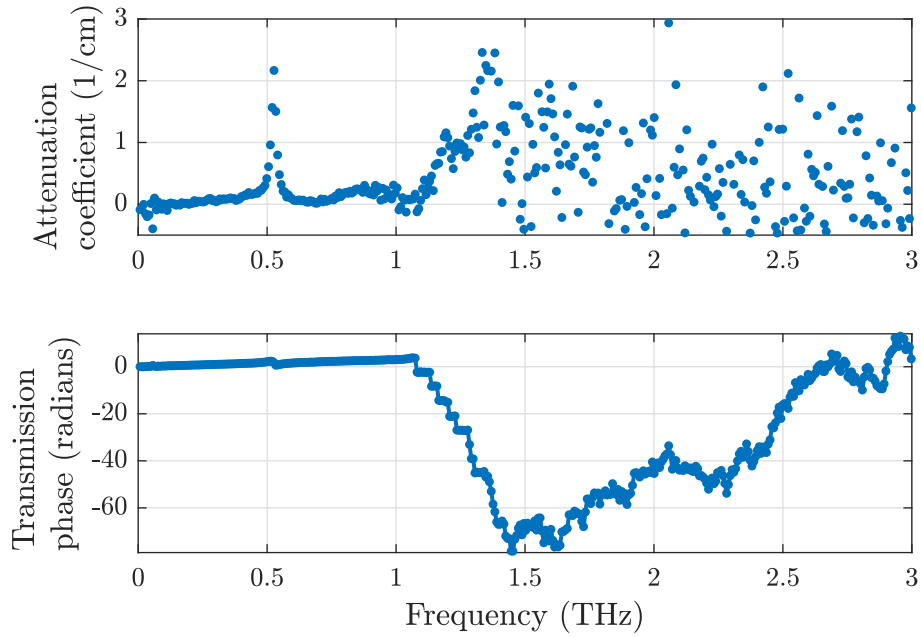


**Figure 3.19:** The attenuation coefficient and the transmission phase computed from the zero padded sample and reference signals.

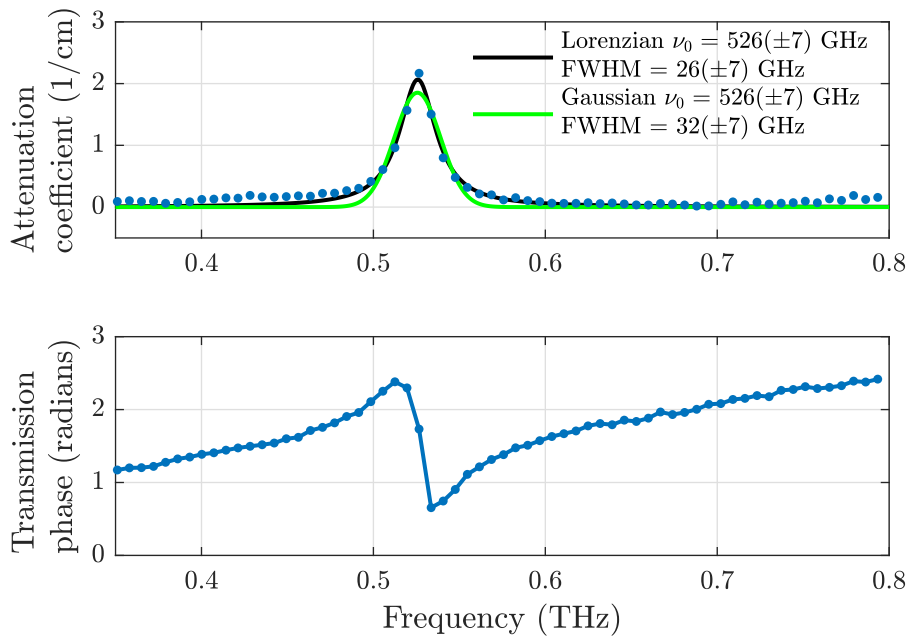


**Figure 3.20:** Zoom in on the 0.53 THz signature of the attenuation coefficient and the transmission phase of the sample computed from the zero padded signals.

### 3.5. Spectrometer Performance

FFT is carried out. The result is shown in Figure 3.19 and a zoom in on the 0.53 signature is shown in Figure 3.20. A clear shift in the frequencies due to the zero padding is appearing, however, both the Gaussian and the Lorentzian line fit predictions are unaffected, and thus, still in good agreement with [19], but a distinct improvement has happened to the transmission phase plot. An explicit resonance is seen at the center frequency at 0.53 THz.

The result of the lactose signature benchmark test is unambiguous. The THz-TDS designed and constructed during the ninth semester in [1] and subsequent optimised in this work functions properly within the limited bandwidth from 0.2 to roughly 1.4 THz. The data analysis is equally carried out correctly to the point of the computations of the Fourier spectrum (spectral amplitude and phase) and the attenuation coefficient given in Eq. (3.2). However, the implementation of the (real) refractive index and the absorption coefficient extraction according to Eqs. (2.83) and (2.84), respectively, is yet to be verified.

### 3.5 Spectrometer Performance

The overall performance of the spectrometer depends on various parts of the setup, however, several things suggest that the THz source is the limiting factor of this spectrometer.

In my ninth semester project [1] it is explained, how a magnified image of the antenna structure can be obtained by light reflected from the antenna, and how this is utilised to align the focal point of the optical beam in the photoconductive gap.

The technique follows; if a beam splitter (be a thin plate of glass tilted  $45^\circ$ ) is inserted close to the lens focusing the optical beam on the photoconductive chip of the THz source, and the focusing lens is shifted a small distance  $x$  from the chip such that the focal point does not cross the surface of the antenna, then an image of the antenna structure will appear on a given screen next to the beam splitter. The situation is sketched in Figure 3.21. This can be understood by the Gaussian lens formula for thin lenses

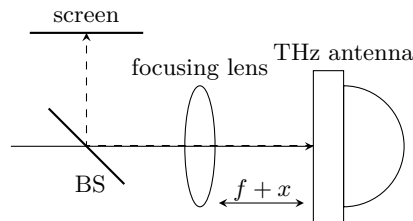


**Figure 3.21:** Illustration of the setup used to get an image of the photoconductive antenna. Figure from [1].

$$\frac{1}{f} = \frac{1}{d_1} + \frac{1}{d_2}, \quad (3.10)$$

where  $f$  is the focal length,  $d_1$  is the object distance, and  $d_2$  is the image distance. The electrodes of the photoconductive antenna are the object at  $d_1 = f + x$ , and the image distance can be calculated as

$$d_2 = \frac{f d_1}{d_1 - f} = \frac{f(f + x)}{x}. \quad (3.11)$$

The magnification  $M$  of the image is then given as

$$M = \frac{d_2}{d_1} = \frac{f}{x}. \quad (3.12)$$

When the photoconductive antenna of the THz emitter is inspected in the reflection, the problem is clear. Figure 3.22 show an image of the photoconductive antenna chip (right)

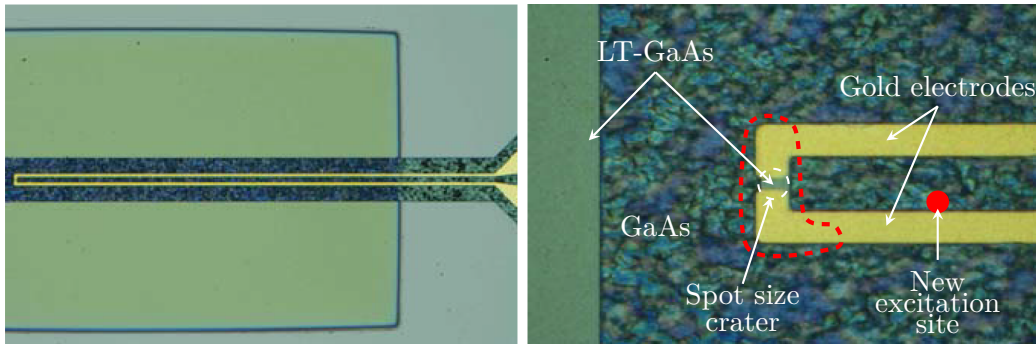


**Figure 3.22:** Image of the chip (right) and a zoom in on the photoconductive gap (left) of the dipole antenna from BATOP Optoelectronics utilised as THz emitter in the spectrometer. The images are taken from [18].

of the emitter and a zoom in on the photoconductive gap (left) taken from the manual [18].

The gold electrodes are no longer present in the area contoured by the dashed red line, and a distinct crater from the optical spot size is located in the photoconductive gap marked by the dashed white contour in Figure 3.22(left). This suggests that the pulse fluence of the incident beam once have been too high resulting a changing temperature gradient causing plastic deformations in the LT-GaAs in the gap and underneath the electrodes. This would explain why the gold electrodes and the LT-GaAs are burst off. These damages have been present during the whole tenth semester, and probaly also been present before the ninth semester, since any pulse from the emitter recorded have had a pulse width  $\sim 10$  ps. Thus, the damages are not likely initiated by the increased pulse fluence operated at during the previous and present semester.

Due to the risk of damaging the THz emitter even further, it should be avoided to focus the optical beam near the damaged area around the photoconductive gap. A single spot is found to work as a new excitation spot marked by the red spot in Figure 3.22(left). This small area may work due to scattering of the LT-GaAs from the shattered gap or due to imperfections of the eching of the LT-GaAs during the fabrication of the antenna. A trace of a THz pulse generated at the new spot is shown in Figure 3.23(top) together with the spectral amplitude (bottom). The trace is a single scan with a predection time constant of 300 ms, a postdetection time constant of 0.1 s, and a software time constant of 3. The scan resolution  $\Delta t$  is 0.17 ps implying a Nyquist frequency  $\nu_c \approx 3$  THz.

The pulse width is unchanged being 10 ps but the pulse shape has changed considerably. The maximum peak intensity is roughly 160 pA, which is much less than the former pulse ( $\sim 480$  pA), but the pulse is more smooth without any odd bumps as the former pulse possessed. Since the excitation spot is shifted relative to the substrate lens and the consecutive collimating lens, the radiated THz beam may not be perfectly collimated. Thus, the THz receiver may miss a part of the radiated THz power. In further work one could test if applying focusing TPX lenses to the THz beam is enough to correct such an effect to any extent.

The frequency spectrum shows a pulse bandwidth of roughly 0.8 THz as before, but the spectral amplitude is clearly cut off around 1 THz indicating a narrowband pulse. The

### 3.5. Spectrometer Performance

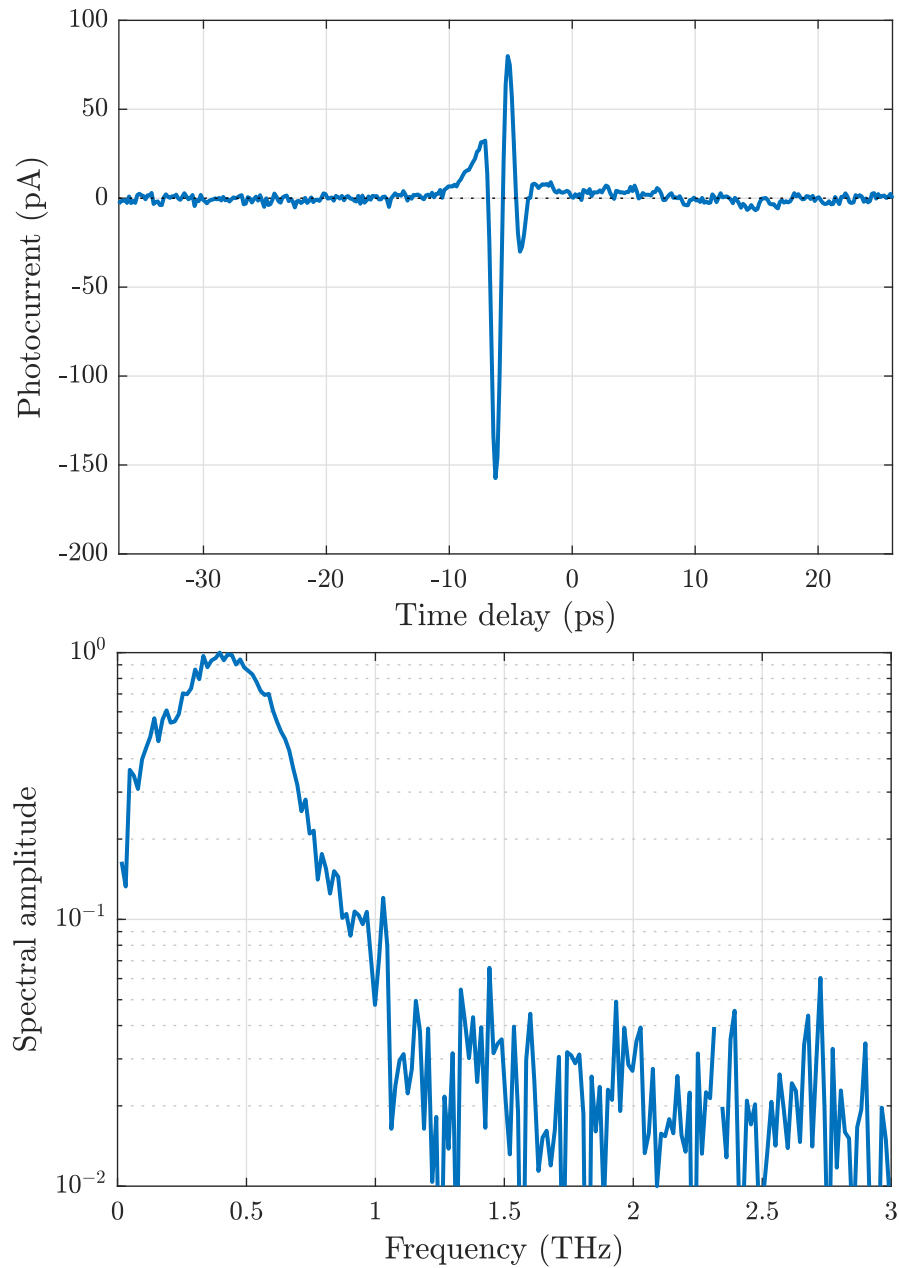


**Figure 3.23:** The time-domain pulse shape (top) and the frequency spectrum (bottom) of a THz pulse generated from the new excitation area marked by the red spot in Figure 3.22(left).

best signal-to-noise ratio of  $\sim 18$  dB is attained at 0.4 THz, however, the ratio decreases quickly above 0.5 THz to less than 8 dB at 1 THz. Taking the long pulse width and the position of the new excitation site into account it may also be, that no LT-GaAs is present and the antenna simply functions as a stripline antenna on GaAs. GaAs has a much longer carrier lifetime, which could explain the longer pulse width.

From the results of these investigations it can be concluded safely, that the THz source is damaged, and therefore it is by far the limiting factor of the designed spectrometer. It is reasonable to believe, that a proper photoconductive THz source based on LT-GaAs would improve signal-to-noise ratio in both the time- and frequency-domain, but also the bandwidth applicable for spectrometric experiments.

## 4. Conclusion and Outlook

During this thesis, the theoretical basis of a complete terahertz time-domain spectrometer setup starting with the interactions of THz radiation and matter through photoconductive generation and detection of broadband THz pulses have been examined thoroughly, but especially, the theory and considerations behind proper data analysis have been elaborated, which have been essential for the construction and optimisation of a functioning TDS.

It was found that the complex refractive index of a sample can be extracted directly from the experimental transfer function if the iterative Newton-Raphson method is applied. Neglecting the etalon effect and only considering low absorptive materials the extraction was simplified to analytic expressions of the (real) refractive index and the absorption coefficient. However, the accuracy is limited in thin samples displaying strong etalon effects.

The study of discrete Fourier transformation revealed how important it can be to choose the right scan resolution in order to avoid aliasing. A relation between the maximum spectral amplitude and the scan duration was indicated but it has not been possible to prove with real data. Instead the maximum amplitude was suggested to be inversely proportional to the scan resolution.

Finally, the theoretical part of this thesis aided a better understanding of lock-in amplifiers, how they should be used, and their limitations.

The experimental work continued the work of my ninth semester project, where the spectrometer was designed and constructed, originally. Essential improvements of both the design and the operation of the spectrometer have, however, been made. The most noticeable improvements were the repair of the THz emitter as well as the upgrade of the retroreflector and the function generator. However, the option that parabolic mirrors can be added also improved the overall usability spectrometer.

Another decisive addition to the spectrometer was the homemade data analysis software written in MATLAB, which eases the handling of large amounts of data.

A set of optimised spectrometer and lock-in settings that should be utilised as default settings, when initiating a new spectrometric measurement, has as well been derived from various tests and accumulated experience.

The main result of this thesis, and the seal of approval of the spectrometer, has been the benchmark characterisation of the strong and narrow absorption signature of  $\alpha$ -lactose monohydrate powder centered around 0.53 THz. The results were clear. The THz-TDS functions properly within the limited bandwidth of the emitter, and the data analysis software written has also been carried out correctly to the extent of the implemented theory.

However, further investigations of the THz emitter exposed damaged antenna electrodes and a missing photoconductive gap resulting in narrowband THz pulses of  $\sim 10$  ps pulse width. These damages are concluded to have arisen prior to both the ninth and the tenth semester, since no stronger or shorter pulses than 10 ps have been detected.

Yet, it can safely be concluded that the constructed and optimised THz-TDS works, and the primary limiting factor is the commercial THz emitter from BATOP Optoelectronics.

## Outlook

Evidently, if future spectrometric experiments are to be made in a rational and reliable way, the THz emitter should be replaced due to the damages.

Instead, an obvious direction of future work would be to characterise different emitter antenna designs in cooperation with the CITS group of AAU led by Esben Skovsen, since the THz detector in the spectrometer is properly functioning.

The damaged THz emitter would then be replaced by the different photoconductive antennas of various designs fabricated in the CITS project. If the PCAs are left without any substrate lenses and a setup of parabolic mirrors, which at least collimates and directs the THz beam to the commercial detector, is installed in the spectrometer, then it would be possible to characterise and compare the different antenna geometries in a systematic and transparent way, independent of distracting errors possibly introduced by misalignment of the substrate lenses ect. Such systematic characterisations of antenna designs and the effects of the antenna parameters are seemingly often neglected, and could thus be interesting to investigate.

## Bibliography

- [1] Mathias Hedegaard Kristensen. Ninth semester project - design and construction of a terahertz time-domain spectrometer, 2016.
- [2] Yun-Shik Lee. Principles of Terahertz Science and Technology. Springer, 2009. ISBN 978-0-387-09539-4.
- [3] K. Sakai (Ed.). Terahertz Optoelectronics. Springer, 2005. ISBN 978-3-540-80023-1.
- [4] Kai-Erik Peiponen, J. Axel Zeitler, and Makoto Kuwata-Gonokami. Terahertz Spectroscopy and Imaging. Springer, 2013. ISBN 978-3-642-29563-8.
- [5] John R. Reitz, Frederick J. Milford, and Robert W. Christy. Foundations of Electromagnetic Theory. Pearson Addison-Wesley, fourth edition, 2009. ISBN 978-0-321-58174-7.
- [6] William H. Press, Brian P. Flannery, Saul A. Teukolsky, and William T. Vetterling. Numerical Recipes in Pascal. Cambridge University Press, 1990. ISBN 0-521-37516-9.
- [7] Eric W. Weisstein. Heaviside step function, 2017. URL <http://mathworld.wolfram.com/HeavisideStepFunction.html>.
- [8] P. U. Jepsen, R. H. Jacobsen, and S. R. Keiding. Generation and detection of terahertz pulses from biased semiconductor antennas. J. Opt. Soc. Am. B, 3(11), 1996.
- [9] Eric W. Weisstein. Convolution theorem, 2017. URL <http://mathworld.wolfram.com/ConvolutionTheorem.html>.
- [10] Truong Khang Nguyen, Won Tae Kim, Bong Joo Kang, Hyeon Sang Bark, Kangho Kim, Jaejin Lee, Ikmo Park, Tae in Jeon, and Fabian Rotermund. Photoconductive dipole antennas for efficient terahertz receiver. Optics communications, 383(50-56), 2017.
- [11] Eric W. Weisstein. Newtons method, 2017. URL <http://mathworld.wolfram.com/NewtonsMethod.html>.
- [12] Peter Uhd Jepsen and Bernd M. Fischer. Dynamic range in terahertz time-domain transmission and reflection spectroscopy. Optics Letters, 30(1), 2005.
- [13] Matthias Hoffmann. Ph.D. thesis: Novel Techniques in THz-Time-Domain-Spectroscopy. Albert-Ludwigs University, Freiburg, 2006.
- [14] Model SR530 Lock-in Amplifier. Stanford Research Systems, 2013. URL <http://www.thinksrs.com/downloads/PDFs/Manuals/SR530m.pdf>.
- [15] About Lock-In Amplifiers - Application Note no. 3. Stanford Research Systems, 2016. URL <http://www.thinksrs.com/downloads/PDFs/ApplicationNotes/AboutLIAs.pdf>.
- [16] Paul Moses. Lock-in Amplifier Overview. Penn State, 2002. URL <http://www.personal.psu.edu/pjm112/PDF/LI.PDF>.
- [17] Instruction manual and data sheet bPCA-100-05-10-800-x. BATOP optoelectronics, 2016. URL [http://batop.de/products/terahertz/photoconductive-antenna/data-sheet/manual\\_bPCA-100-05-10-800.pdf](http://batop.de/products/terahertz/photoconductive-antenna/data-sheet/manual_bPCA-100-05-10-800.pdf).

- [18] Instruction manual and data sheet PCA-40-05-10-800-x. BATOP optoelectronics, 2016. URL [http://batop.de/products/terahertz/photoconductive-antenna/data-sheet/manual\\_PCA-40-05-10-800.pdf](http://batop.de/products/terahertz/photoconductive-antenna/data-sheet/manual_PCA-40-05-10-800.pdf).
- [19] E. R. Brown, J. E. Bjarnason, A. M. Fedor, and T. M. Korter. On the strong and narrow absorption signature in lactose at 0.53 thz. Applied Physics Letters, 90 (061908), 2007.
- [20] Eric W. Weisstein. Lorentzian function, 2017. URL <http://mathworld.wolfram.com/LorentzianFunction.html>.
- [21] Eric W. Weisstein. Gaussian function, 2017. URL <http://mathworld.wolfram.com/GaussianFunction.html>.